

Fig. V.51. USb s.c. A log-log plot of reduced magnetization M/M_0 against reduced temperature, t , [78LSSV]. $M/M_0 = D(1-T/T_N)^\beta$; $D = 1.33(5)$; the value $\beta = 0.32$ corresponds to the 3D Ising systems ($\beta = 0.3125$). $T_N = 241.17(5)$ K (see LB III/12c, p.430, Fig. 48).

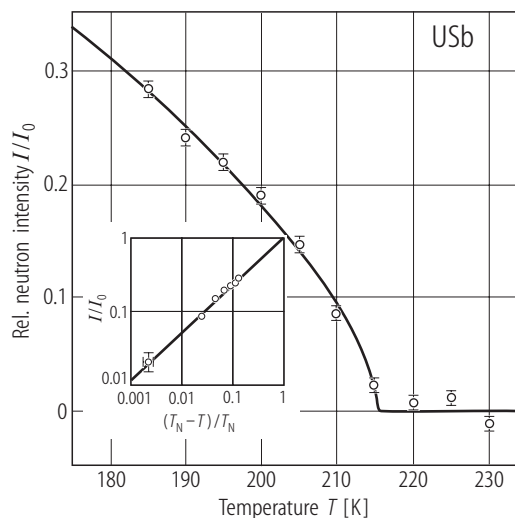
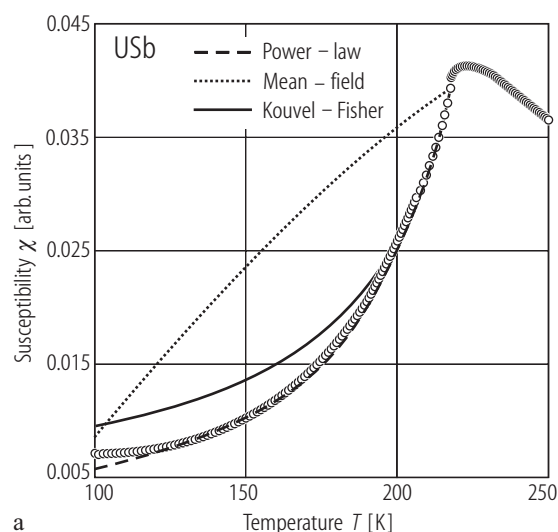
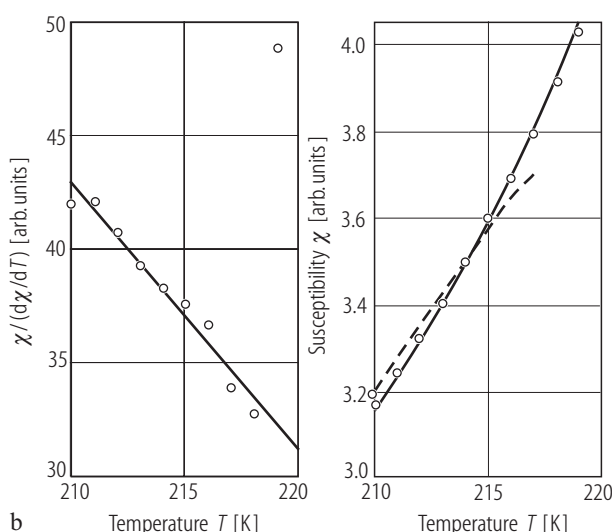


Fig. V.52. USb. Powder neutron diffraction intensity ratio, I/I_0 , of the AF (210) reflection as a function of temperature, T , near $T_N (= 215.5(5)$ K) [02NPSM]. $I \sim t^{2\beta}$, where the experimental $\beta (= 0.33(5))$ value is close to the 3D-Heisenberg value of 0.367. A log-log plot of I/I_0 vs. t is shown in the inset.



a



b

Fig. V.53. USb s.c. (a) Magnetic susceptibility, χ , along the [111] direction as a function of temperature, T , compared to theoretical treatments [02NPSM]. $T_N (= 217.7(5)$ K) found from the maximum slope of $\chi(T)$. The power-law $\chi \sim t^\gamma$ gives $\gamma = 1.3(2)$ found between 130 and 210 K. Mean field approximation is for $\gamma = 1$. In the case of Kouvel-Fisher (KF) treatment, γ is deduced from the slope of $\chi/(d\chi/dT)$ vs. T .

(b) Left-hand panel: The straight-line KF fit in the range 210...218 K yields $\gamma = 1.2(2)$. The Monte Carlo value for 3D-H is 1.270(1). Right-hand panel: Comparison between power-form (dashed-line) and KF methods (solid-line) in the critical region. Note that the latter fit is followed for all the critical region data, while the former one only for lower T range.

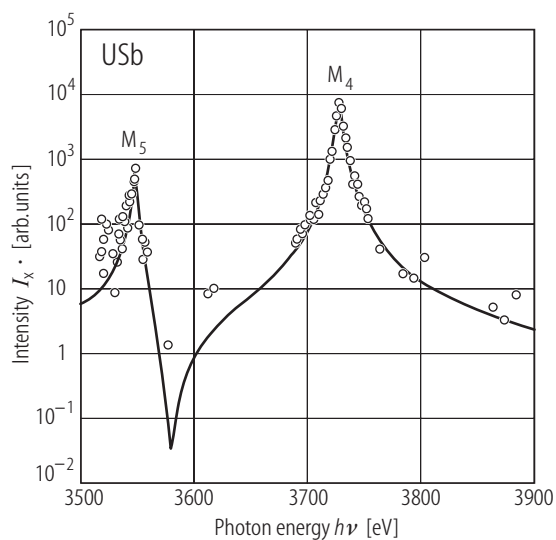


Fig. V.54. USb s.c. RXMS: Intensity of scattering X-rays I_x (log-scale) vs. the photon energy $h\nu$ [92TSLG]. The solid line is a fit to two resonance dipole models as inferred from atomic physics. They are located at the absorption edges and Lorentzian in form. The resonances correspond to those at the M_5 and M_4 edges.

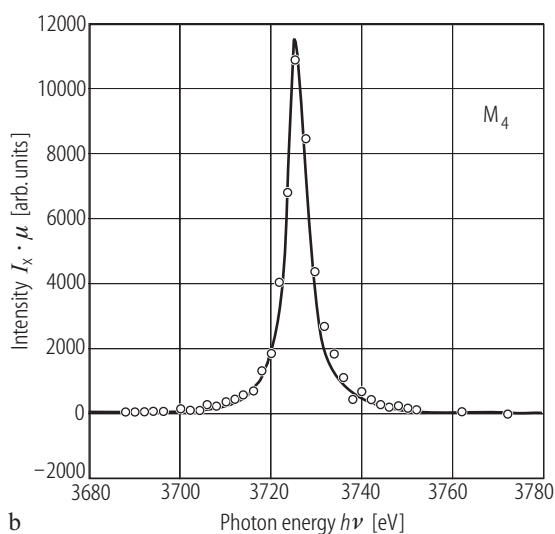
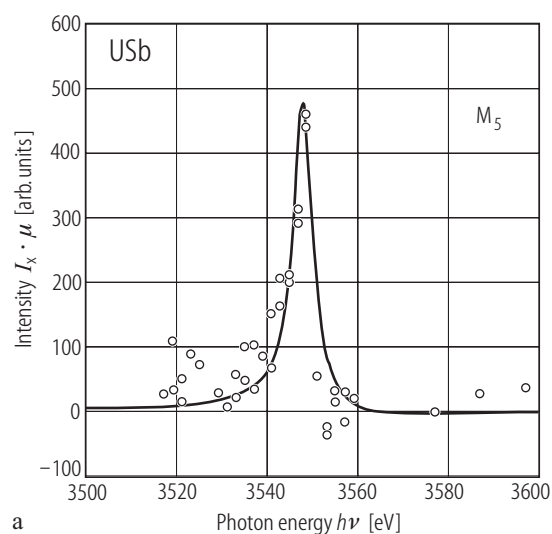


Fig. V.55. USb s.c. RXMS: Energy dependence of the integrated X-ray intensity, I_x , of the (001) magnetic reflections at 12 K for the two resonance edges: **(a)** M_5 and **(b)** M_4 [92TSLG]. The solid lines are fits of the M_5 and M_4

data using standard formulas for atomic resonances, where these are considered as two resonances of M_4 - and M_5 -edges, each with amplitudes A_4 and A_5 , with widths Γ_4 and Γ_5 and energies E_4 and E_5 , respectively.

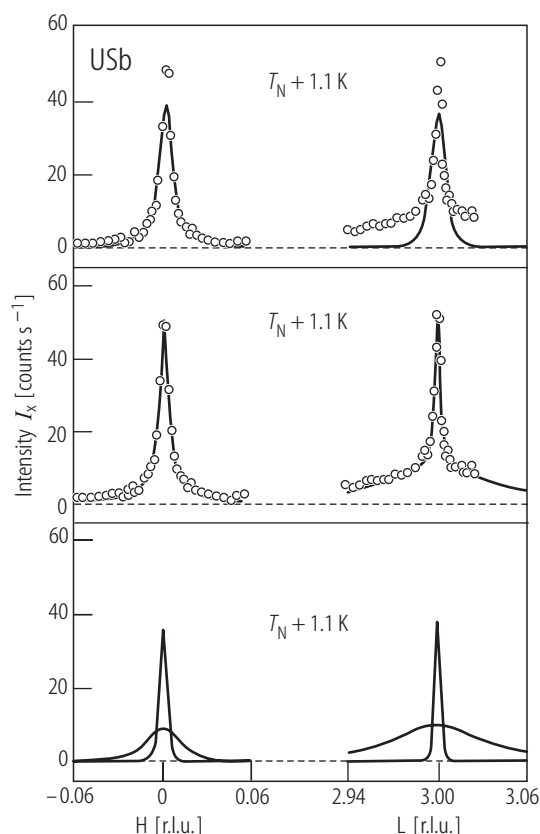


Fig. V.56. USb s.c. RXMS: Two component critical scattering above T_N (middle panel) [96PNSL]. The solid line is the best fit to the sum of Lorentzian (L) and a squared-Lorentzian (L^2) function convoluted with the instrumental resolution, which represents the “broad” and “narrow” component, respectively. The top panel shows the unsatisfactory description by a single component only. The lower panel shows the separate components used in the fit. Measurements were made with reciprocal-space scans in the H and L directions.

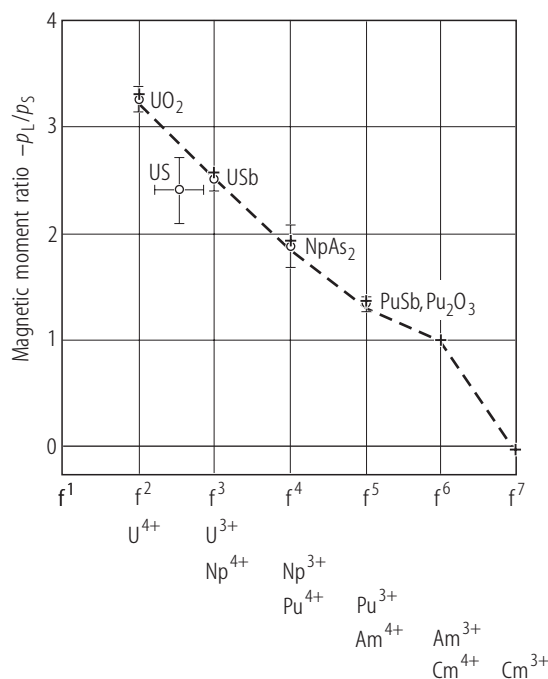


Fig. V.57. AnSb (An = U, Pu). The ratio of the orbital (p_L) and spin (p_S) components of the magnetic moments as a function of the number of $5f$ electrons (f^n). The mononictides USb ($n = 3$) and PuSb ($n = 5$) are compared to the mostly ionic compounds UO_2 ($n = 2$) and Pu_2O_3 ($n = 5$) as well as to semimetal $NpAs_2$ ($n = 4$) [93L3]. All these were inferred by analyzing the shape of the magnetic form factor determined by polarized neutrons. The values for typically metallic compounds like AnT_2 ($T = Fe, Co, Ni$) and ternary compound $URhAl$ are not displayed for clarity. The crosses are the free-ion values in intermediate coupling, which are connected by the dashed line. Within a single J term ($^{2s+1}L_J$) whatever the CEF state, p_L/p_S is the same and related to the Landé factor g , $p_L/p_S = (1-g/2)/(g-1)$.

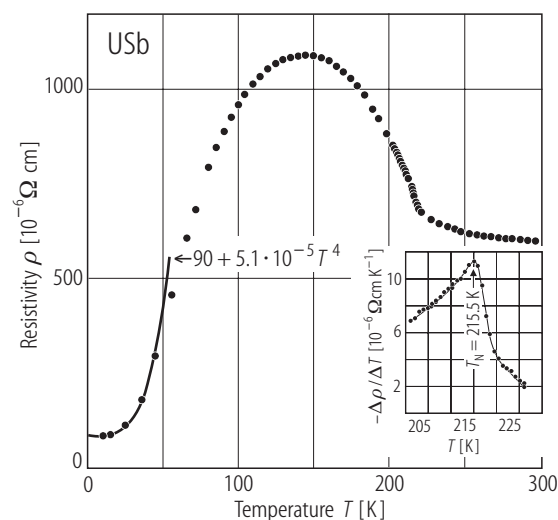


Fig. V.58. USb s.c. Electrical resistivity, ρ , vs. T at 2...300 K and in zero field. Solid line is a T^4 power-law fit up to 45 K. A $C_m T^2 \exp(-\Delta/T)$ fit is also possible (for parameters see Table 4) [84SFV]. Δ is the magnon activation energy. The $n = 4$ coefficient is ascribed to be scattering of the carriers on the spin waves of linear dispersion. Note a logarithmic decrease of $\rho(T)$ for $T > T_N$. Inset: The derivation of T_N ($= 215.5(1)$ K) from the maximum of the $\Delta\rho(T)/\Delta T$ curve.

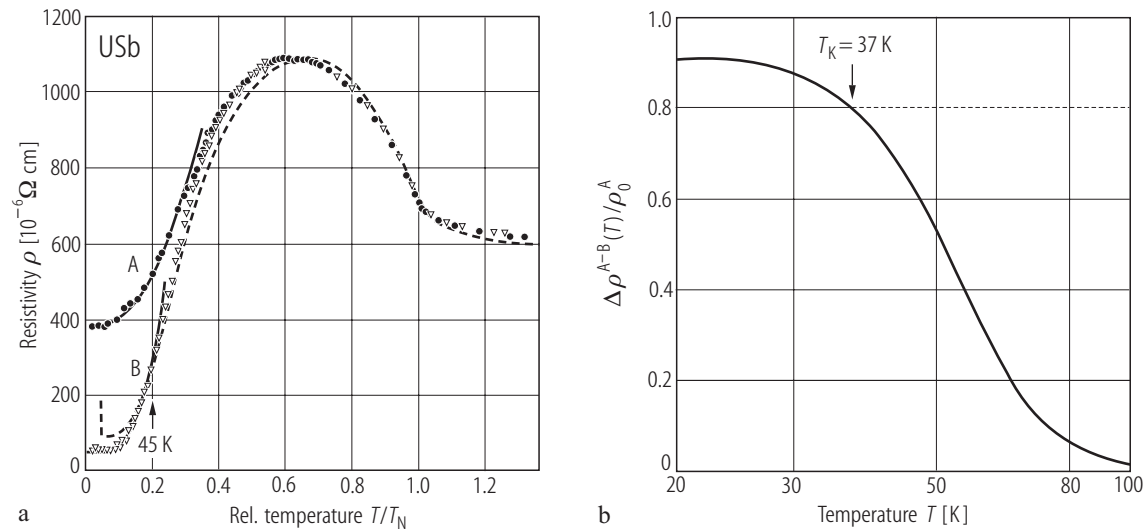


Fig. V.59. USb s.c. **(a)** Electrical resistivity, ρ , vs. T/T_N for two crystals A (full circles- $a = 0.6198(2) \text{ nm}$, $T_N = 211.2 \text{ K}$, $RR = 1.6$) and B (open triangles- $a = 0.6205(2) \text{ nm}$, $T_N = 218.7 \text{ K}$, $RR = 13$) [95HW] and [01WH] compared to that dependence reported for USb ($T_N = 215.5 \text{ K}$) in [84SFV] (dashed line), see Fig. V.58. The $\rho(T)$ data for the sample B were multiplied by a constant factor to meet the data of [84SFV] at $T/T_N = 1$. $\rho_{RT} = 580 \mu\Omega\text{cm}$. The power-law dependencies of the resistivity T^n with $n = 2.4$ and 3.7 for the A and B samples, respectively, are marked by solid

lines. Note a difference of $330 \mu\Omega\text{cm}$ at 4.2 K in ρ between the samples A and B. **(b)** The resistivity difference $\Delta\rho^{A-B}$, between the $RR = 1.6^{(A)}$ and $13^{(B)}$ samples divided by the resistivity $\rho_0 (\approx \rho^A(4.2 \text{ K}))$ of the $RR = 1.6$ sample as a function of $\log T$ [01WH]. The Kondo temperature $T_K = 37 \text{ K}$ is found for the $\Delta\rho/\rho_0 = 0.8$ value. Note that below T_K the Kondo resistivity tends to saturation according to the Fermi-liquid formula: $\rho_K(T) = \rho_K(0)[1 - (T/T_K)^2]$ (see also Fig.V.61).

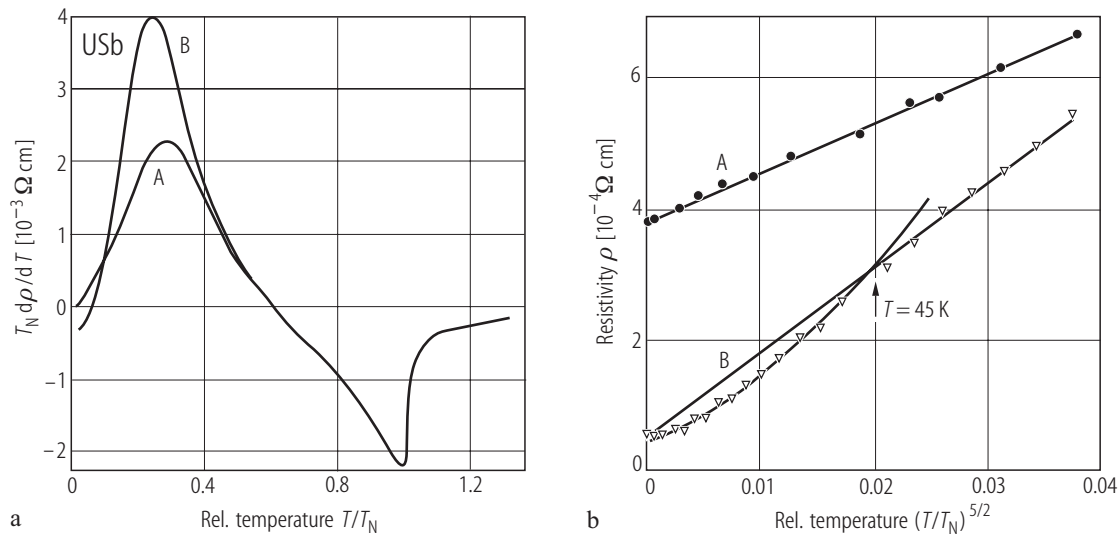


Fig. V.60. USb s.c. **(a)** Temperature derivative of the resistivity multiplied by T_N , $T_N d\rho/dT$ vs. (T/T_N) for samples A and B (see Fig.V.59) [95HW]. **(b)** Electrical resistivity of samples A and B vs. $(T/T_N)^{5/2}$ in the range ca. $2 \dots 60 \text{ K}$ [95HW]. Solid straight lines represent the best fit by the l.l.s. sum method. The deviation of $\rho(T/T_N)$ from the

straight line for sample B at $T < 45 \text{ K}$ is assumed to the phonon/magnon drag effect on the resistivity being inversely proportional to the carrier concentration. This interpretation has been changed into the so-called TLS effect in [01WH] (see Fig. V.67).

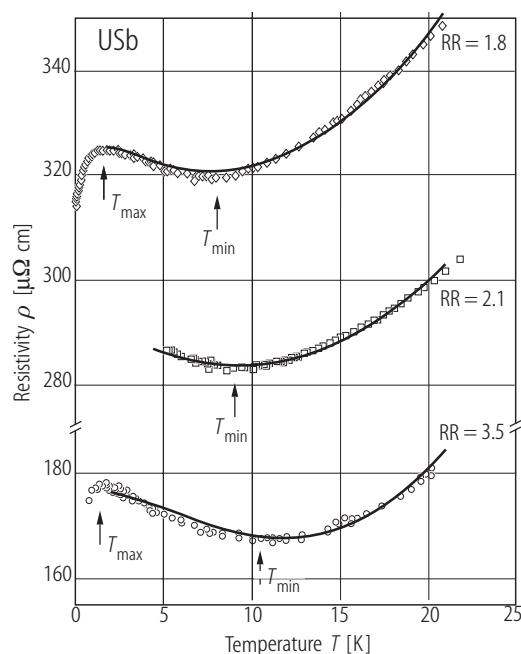


Fig. V.61. USb s.c. Low-temperature electrical resistivity ρ for three single crystals with different RR from 1.8 to 3.5 as a function of temperature, T , [01WH]. The solid lines are fittings of the experimental data to the equation containing three contributions: $\rho(T) = \rho_0 + \rho_K(T) + \rho_m(T)$ determined between 1.2 (T_{\max}) and 20 K. $T_K = 37$ K. The magnon resistivity $\rho_m(T) = bT(1+2T/\Delta)\exp(-\Delta/T)$ where ρ_0 , $\rho_K(T)$, b and Δ are sample dependent. The gap Δ changes from 11.8 to 28.2 K for the samples of RR = 1.8 and 3.5 respectively. The low-temperature resistivity maximum is interpreted as the onset of the coherence effect for a high Kondo impurity concentration.

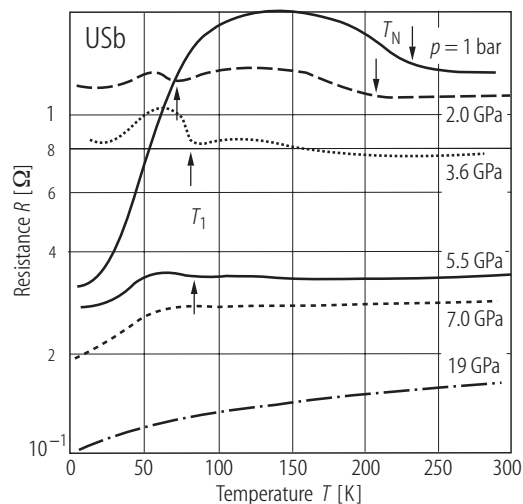
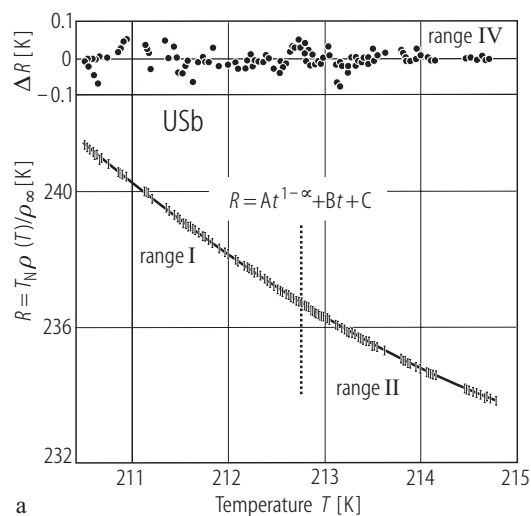
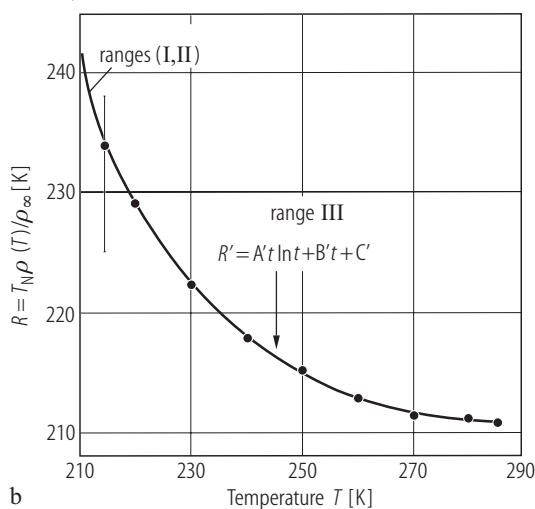


Fig. V.62. USb s.c. Electrical resistance as $\log R$ vs. temperature, T , under various applied pressures, p , indicated [96BGM]. Below 2 GPa the onset of the $3k$ -type structure at temperature T_N shifts as -17 K/GPa. Between 2 and 6 GPa a second anomaly appears at T_1 (see reversed arrows). Above 6 GPa no anomaly exists and no changes in the curve shape of $R(T)$ is observed up to a maximum pressure measured (23 GPa).

Fig. V.63. USb s.c. Electrical resistivity vs. T along the [110] crystal axis in critical regions above T_N ($= 210.3$ K) [95HW], [96WH]. The solid curves are best fits of the data to the equations: (a) $R(T) = At^{1-\alpha} + Bt + C$, where $t = (T - T_N)/T_N$ and $A = -315(11)$ K $[-66(5)$ K], $C = 243$ K [248 K] and $\alpha = 0.090(8)[0.60(5)]$ for range I ($1 \cdot 10^{-3} < t < 1.15 \cdot 10^{-2}$) and [range II] ($-1.15 \cdot 10^{-2} < t < 0.02$) respectively, where B ($= 16.3$ K) was fixed for both ranges, and (b) $R'(T) = A't \ln t + B't + C'$, where $A' = 82(2)$ K, $B' = 0(2)$ K and $C' = 242.6(3)$ K for range III ($0.02 < t < 0.35$). Note that the data obtained for range I are in the critical temperature range. Range IV (figure a) represents the deviation ΔR of the experimental data from the fitted function.



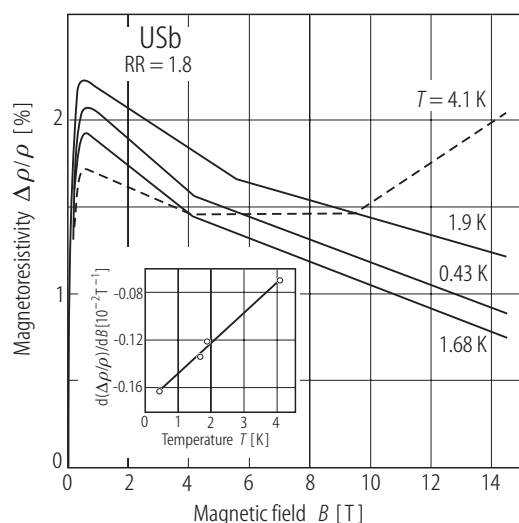


Fig. V.64. USb s.c. Transverse magnetoresistivity vs. magnetic field, B , measured at low temperature between 0.4 and 4.1 K along $[110]$, around low temperature T_{\max} (see Fig. 61) for the sample with $RR = 1.8$ [01WH]. The electrical current was directed along the $[\bar{1}\bar{1}1]$ axis. Inset: The magnetic field derivative $d(\Delta\rho/\rho)/dB$ vs. T at very low temperatures.

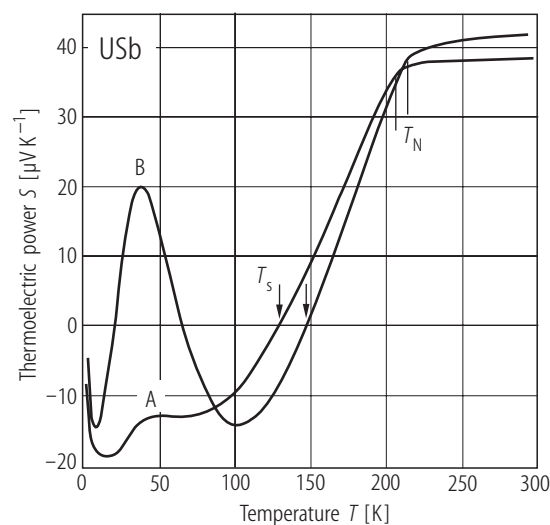


Fig. V.66. USb s.c. Thermoelectric power, S , vs T for single crystals A and B (see Fig. V.59) oriented along the $[100]$ axis [95HW]. $S_{RT} = 38.8 \mu\text{V/K}$ and $42.1 \mu\text{V/K}$ for A and B, respectively. The sign change is at T_S (see arrows) similar to that of $R_H(T)$, observed by [84SFV] (see Fig. V.69). The low-temperature peaks are due to the magnon drag phenomenon being greatly reduced by impurities and disorder as in sample A.

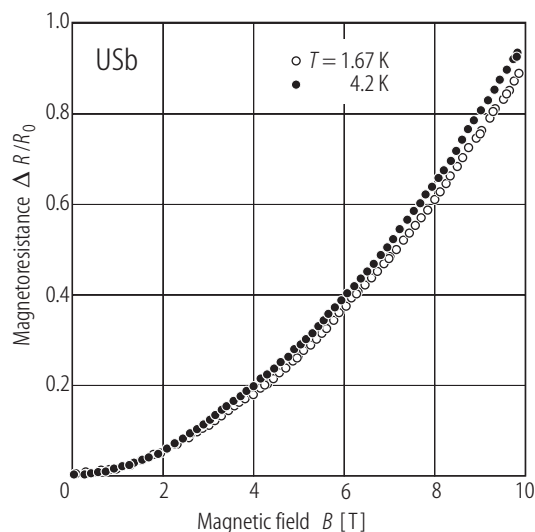


Fig. V.65. USb s.c. Magnetoresistance, $\Delta R/R_0 = (R(B) - R_0)/R_0$, vs. B at 1.67 K (open circles) and 4.2 K (closed circles), measured up to 10 T [94SWOS].

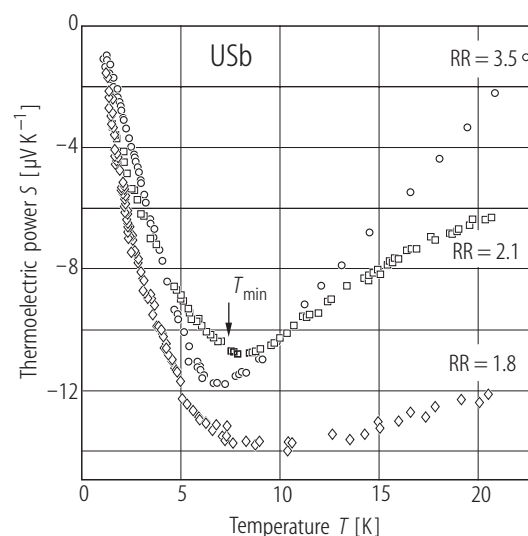


Fig. V.67. USb s.c. The low-temperature thermoelectric power, S , for samples having different RR as a function of temperature [01WH]. The T_{\min} values increase with decreasing RR value from 7 to 9 K for the samples with $RR = 3.5$ and 1.8 , respectively. These curves are the result of competition between two effects: the first one is due to the band reconstruction and leads to an increase in intrinsic – negative $S(T)$ with decreasing T . The extrinsic second effect is positive and sensitive to the defect density. This behaviour is probably the realization of a two-level system (TLS) scattering effect and are not caused by usual single – impurity Kondo interaction met in magnetic materials.

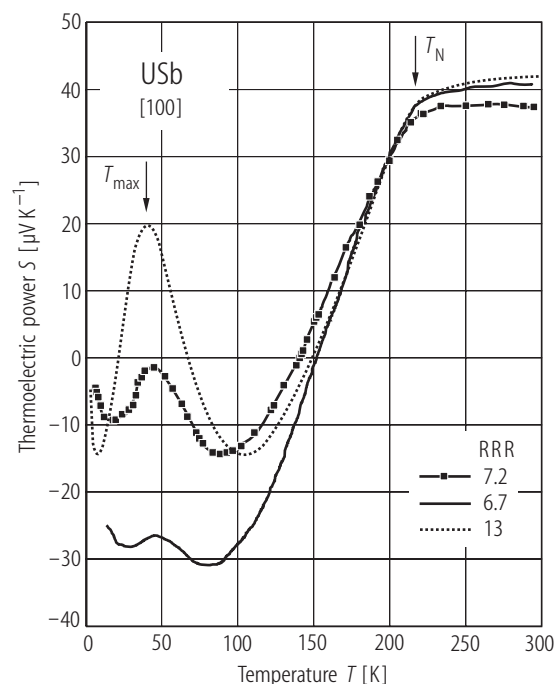


Fig. V.68. USb s.c. Thermoelectric power, S , vs. temperature, T , of USb single crystals. Samples are characterized by different RRR ratios. Sample with RRR = 7.2 from [05TSMC] is compared to earlier investigations of [85FSV2] (RRR = 6.7) and [95HW] (RRR = 13). Note a change of sign around $T \approx 150$ K and a double structure with a peak at about 40...50 K. Note also a rather high RT value of S ($\approx +40$ $\mu\text{V/K}$). The 40...50 K peak is probably caused by the phonon/drag thermoelectricity S_g , which is usually greatly reduced by impurities and disorder [95HW].

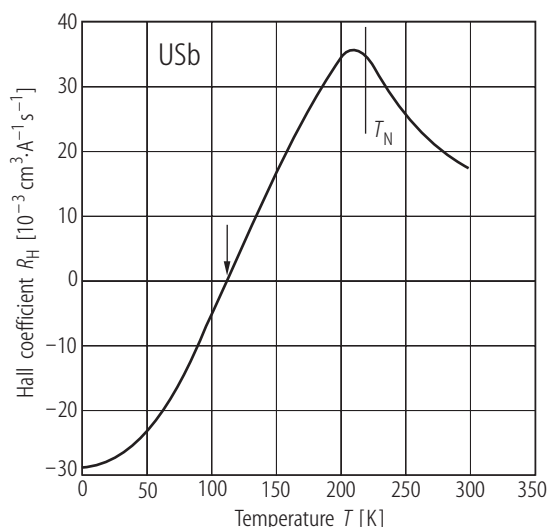


Fig. V.69. USb s.c. The total Hall coefficient, R_H , vs. T [84SFV]. The Hall resistivity $\rho_H = R_H H$ was found to increase linearly with magnetic field up to 10 T (not shown). This does not allow to break down R_H -total into ordinary R_0 and extraordinary R_s parts. In a one-band model R_0 is assumed to correspond to about 0.02 e/FU. See also [94OSSS].

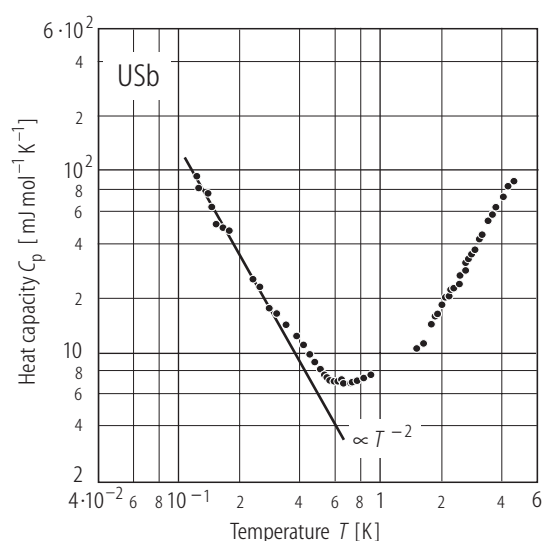


Fig. V.70. USb s.c. A double log plot of the heat capacity, C_p , vs. temperature, T , between 0.1 and 5 K [83RFOV]. The solid line through the points below 0.3 K shows the expected T^{-2} behaviour for nuclear contribution, C_N , from hyperfine-split levels of ^{121}Sb and ^{123}Sb nuclei with nuclear spins of $I = 5/2$ and $7/2$, respectively.

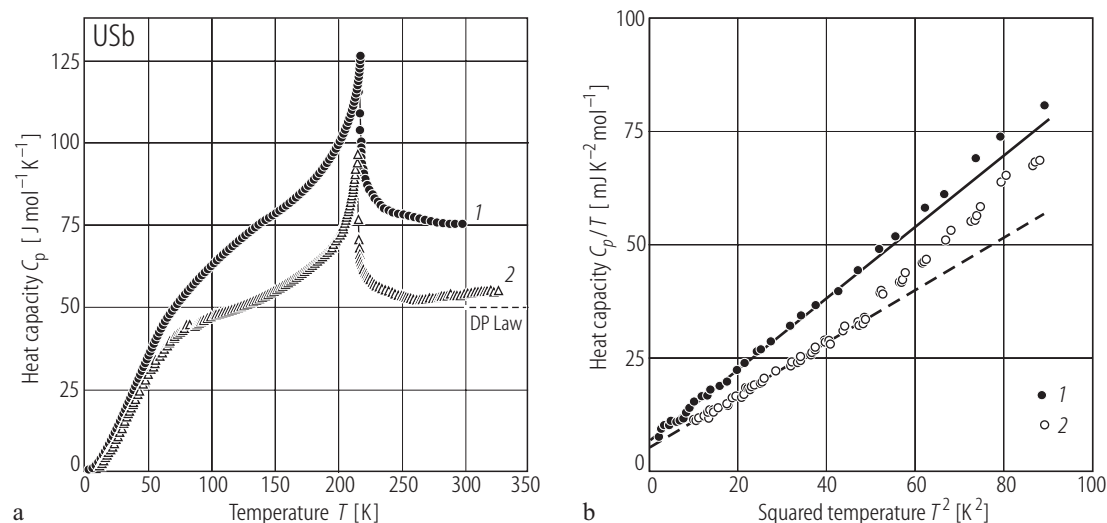


Fig. V.71. USb s.c. **(a)** Heat capacity, C_p , vs. temperature, T , measured by different authors: curve 1) [94OSSS] and 2) [05TSMC, 85ROV2]. Note that the C_p value of the former authors being equal to 75 J/K mol at 300 K exceeds considerably the Dulong-Petit (DP) value of 50 J/K mol. The small peak at 83 K in the $C_p(T)$ curve of the latter

authors is due to a small contamination of a single crystal by the U_5Sb_4 ferromagnet. **(b)** The low-temperature C_p/T vs. T^2 dependence measured by 1) [85ROV2] and 2) [05TSMC]. Note that despite the differences in absolute values of C_p both dependences give $\gamma(0) = 4.5 \text{ mJ/mol K}^2$.

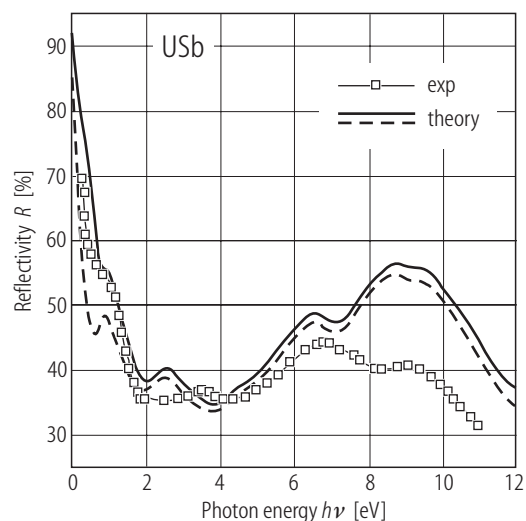


Fig. V.72. USb. Calculated and experimental reflectivity spectrum, R , vs. photon energy, $h\nu$, [05KO]. The dashed curve gives the *ab initio* calculated reflectivity without the intraband Drude contribution, while the solid curve gives the *ab initio* calculated reflectivity including a phenomenological Drude term (with $\sigma_D = 3 \cdot 10^{15} \text{ s}^{-1}$, $\delta_D = 0.45 \text{ eV}$). The experimental data (open squares) are from [79SV] shown in Fig. V.73a.

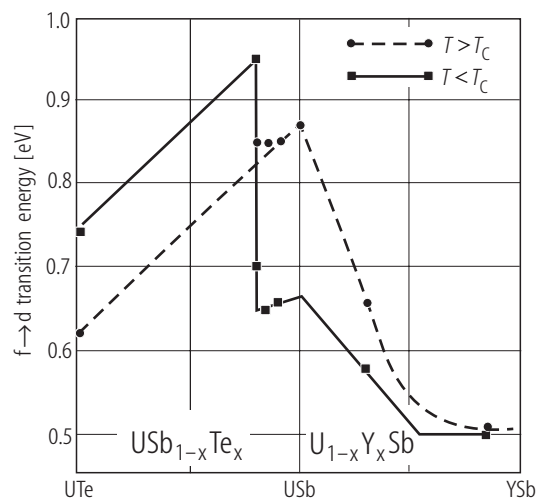


Fig. V.74. (U,Y)Sb, U(Sb,Te). Comparison of that part of the $f \rightarrow d$ transition energy in the solid solutions $\text{U}_{1-x}\text{Y}_x\text{Sb}$ and $\text{USb}_{1-x}\text{Te}_x$ being at magnetically ordered and disordered states [86R]. Note that the transition energy is highest for USb. The decrease from USb to UTe is due to the increase of the Fermi energy (1 more d electron), while going from USb to YSb, E_F is not changed relative to the d-band but the strength of p-f hybridization decreases. The effect of diluting Y in USb corresponds to pushing down the VB due to decreasing of the p-f mixing energy and the f states are closer to E_F . This is in agreement with UPS results [82RMV] (see Fig. V.22).

For Fig. V.73 see next page

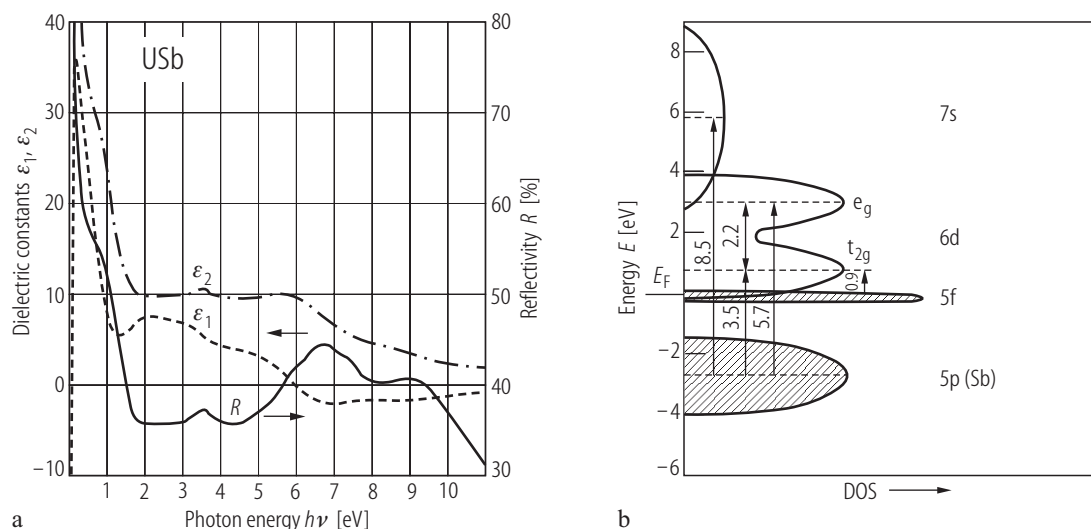


Fig. V.73. USb s.c. **(a)** The near normal incidence reflectivity R (rhs) and the real (ϵ_1) and imaginary (ϵ_2) parts of dielectric functions (lhs) at RT, both as a function of photon energy $h\nu$ [78SV], [79SV]. Note a huge peak at 0.1 eV and a smaller one at 2.2 eV in ϵ_1 and two prominent peaks at 3.4 and 5.6 eV in ϵ_2 as well as a clear structure in

the optical conductivity $\text{Re } \sigma$ denoted as R . The maxima in $\text{Re } \sigma$ are related to the electronic transitions between the DOS. **(b)** Energy level scheme of USb derived on the base of the above mentioned optical investigations [78SV], [79SV]. Numbers are in eV units.

For Fig. V.75 see next page

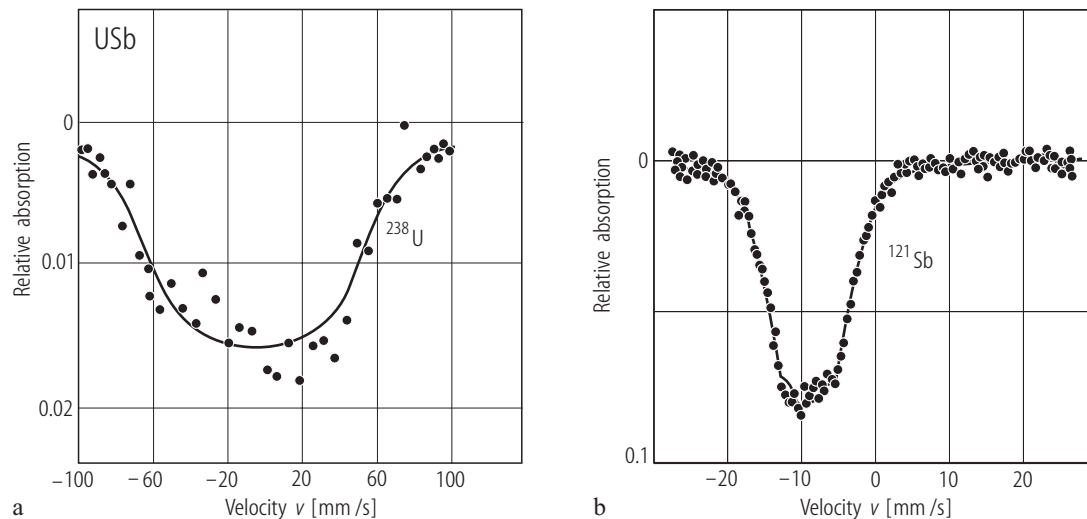


Fig. V.76. USb. **(a)** The NGR spectrum of the ^{238}U resonance taken at 4.2 K [70SKRD]. The resulted spectrum consists of five equally intense and spaced lines without resolving due to the large width of the resonance. The solid line is a fit of the data points for a magnetic interaction energy: $\mu_{\text{N}} g_{\text{ex}} H_{\text{hf}}(\text{U})/I = 24(1)$ mm/s. For $g_{\text{ex}} = 0.25$, $\mu_0 H_{\text{hf}}(\text{U}) = 450(20)$ T at the uranium nucleus. **(b)** The NGR

spectrum of ^{121}Sb taken at 4.2 K [70SKRD]. The solid line is a fit to the data for ^{121}Sb hf-magnetic field of $\mu_0 H_{\text{hf}}(\text{Sb}) = 17.0(5)$ T at the antimony nuclei. The isomer shift relative to an InSb standard absorber, IS, is $0.10(5)$ mm/s. The $H_{\text{eff}}(\text{U})$ and $H_{\text{eff}}(\text{Sb})$ are in agreement with the coefficient a_2 found in an analysis of C_N for USb ([85ROV2]), see Fig. V.70.

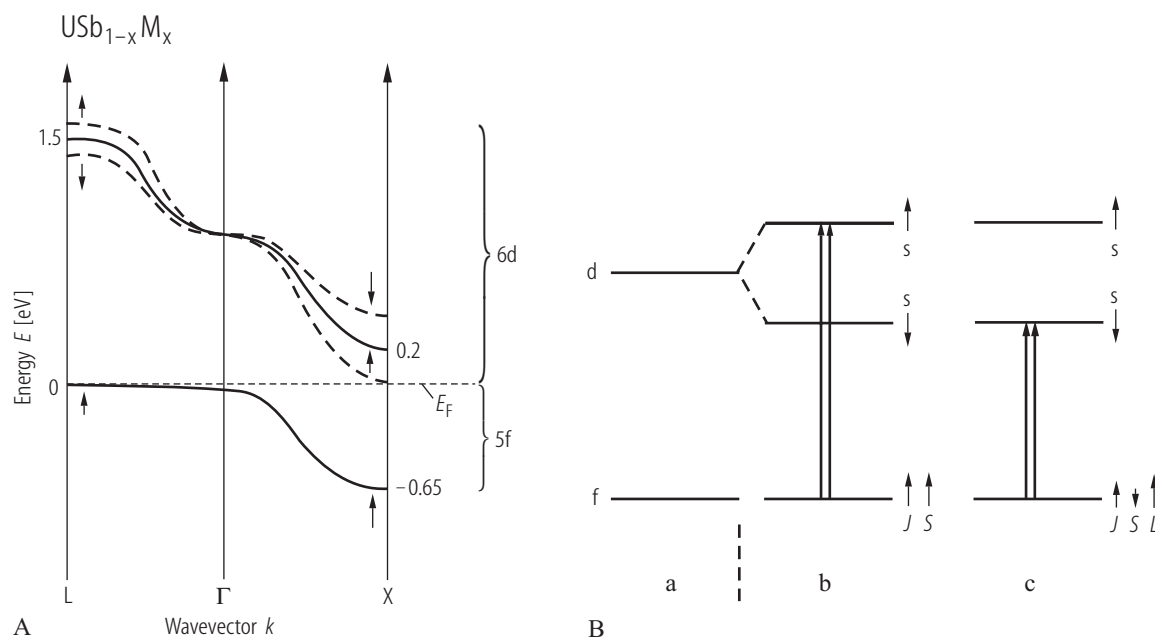


Fig. V.75. U(Sb,M). **(A)** General band model of f and d-states in the vicinity of E_F in some solid solutions U(Sb_{1-x}M_x) in the Γ -X and Γ -L directions [86R]. Within this model the occupied f-band lies at E_F at certain symmetry points of BZ (e.g. at L and Γ points). The situation is different e.g. at the X point, where due to the strong p-f hybridization the f-band is pulled away from E_F . Also the d-bands in fcc symmetry have the lowest energy at the X and the highest at the L-point. The d-band shifts to higher energies due to the successive filling of the d states by excessive d electrons. Whereas the f band is pinned at E_F independently of the composition x, e.g. in the solid solutions U(Sb,M) because the number of f electrons is

approximately constant in the solid solutions with an (M)-atom (in case of M = Te one more d-electron). The arrows show the direction of the moments in both cases, i.e. for the f and spin polarized d-subbands below $T_{C,N}$. This scheme leads to a red-shift of the transition at X and a blue-shift at L as shown below. This picture is corroborated by several band structure calculations, e.g. by [82WPN] or [84B2,3]. **(B)** Scheme of atomic f and d states in situations: **(a)** unmagnetized and **(b), (c)** magnetized. The dominance of a spin results in a blue-shift **(b)** while that of an orbital moment results in a red shift **(c)**. For details see corresponding papers.

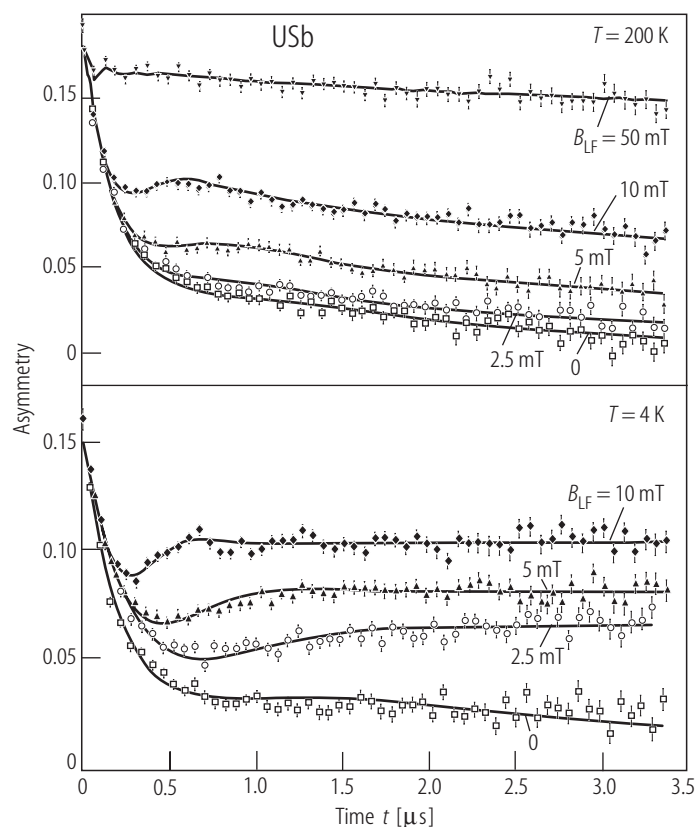


Fig. V.77. USb. Longitudinal field (LF) decoupling μ SR spectra (asymmetry) below T_N at 200 and 4 K [90AKKL]. The solid lines are fits to a dynamic Lorentzian Kubo-Toyabe function with a static width Δ and modulation rate $1/\tau$ as physical parameters. At 200 K, Δ remains constant in magnetic fields but at 4 K it decreases by about 15% in longitudinal field between zero and 10 mT. With increasing magnetic field the spectra become more static.

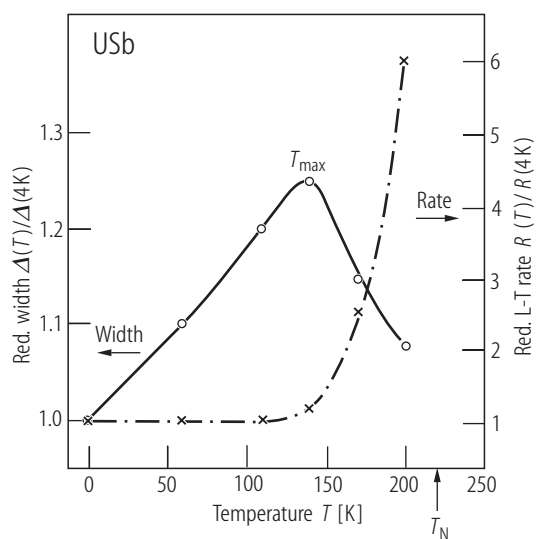


Fig. V.78. USb. μ SR: Reduced, both static width, $\Delta(T)/\Delta(4\text{ K})$, (lhs) and the rate of Lorentzian-Toyabe (L-T) spectra, $R(T)/R(4\text{ K})$, (rhs) vs. temperature, T , determined in the antiferromagnetic region [90AKKL]. A maximum in the function $\Delta(T)$ at 140 K is associated to a sudden increase in the modulation rate $1/\tau$ and relates to a collapse in neutron scattering into broad inelastic scattering peaking at zero frequency [88HSL]. This effect is due to the diffusion of pseudoexcitations related to the phase delocking of the components of the triple- k structure. Close to this temperature ($T^* = 143\text{ K}$) the effect of depolarization of the polarized neutrons has been reported (see Fig. V.36).

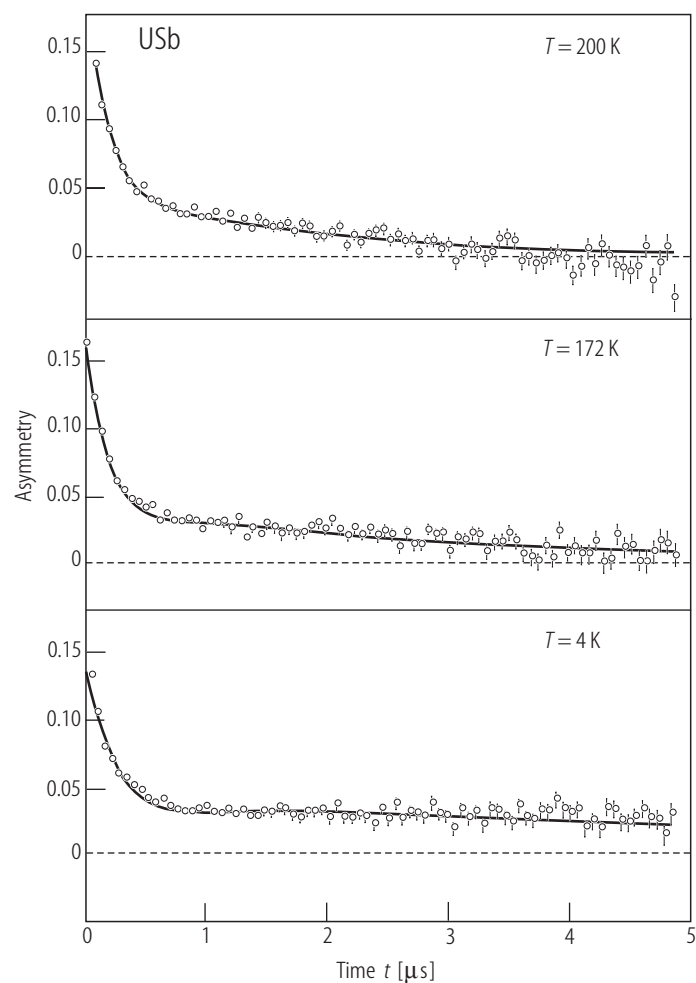


Fig. V.79. USb. Zero field μSR spectra of USb at three indicated temperatures below T_N ($= 240 \text{ K}$). The solid lines are fits to a dynamic Lorentzian Kubo-Toyabe function with static width Δ and modulation rate $1/\tau$ as physical parameters [90AKKL].

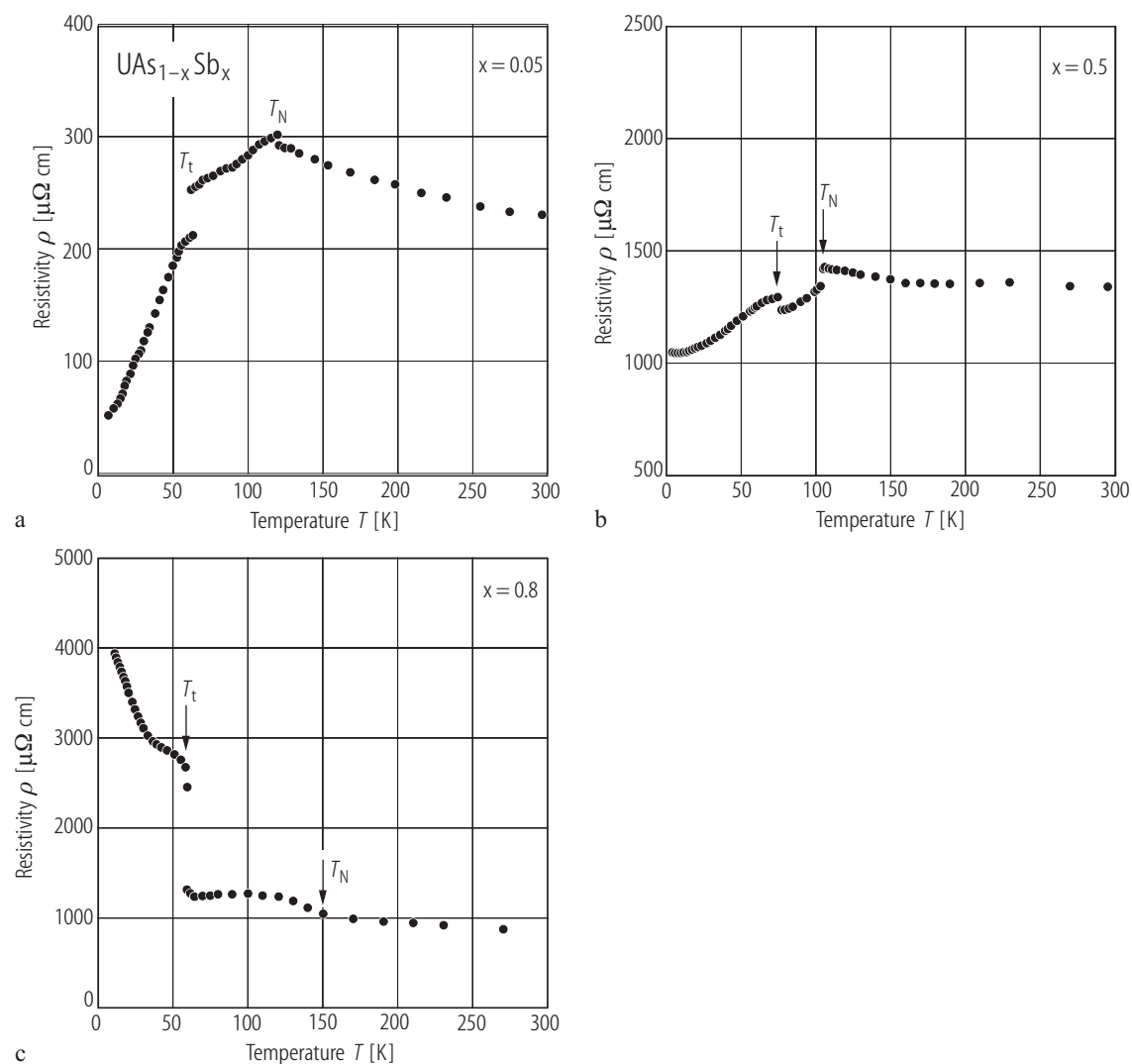


Fig. V.80. U(As,Sb) . Electrical resistivity, ρ , vs. temperature, T , for the solid solutions $\text{UAs}_{1-x}\text{Sb}_x$ **(a)** $x = 0.05$, **(b)** $x = 0.50$, and **(c)** $x = 0.80$ [87ROFV]. For transition temperatures and $\rho(\text{RT})$ -values see the Table:

x	T_t [K]	T_N [K]	$\rho(\text{RT})$ [$\mu\Omega\text{cm}$]
0.05	61(1)	121(1)	220
0.50	77(1)	105(1)	1400
0.80	55*)	150(10)	900

*) a jump in $\rho(T)$

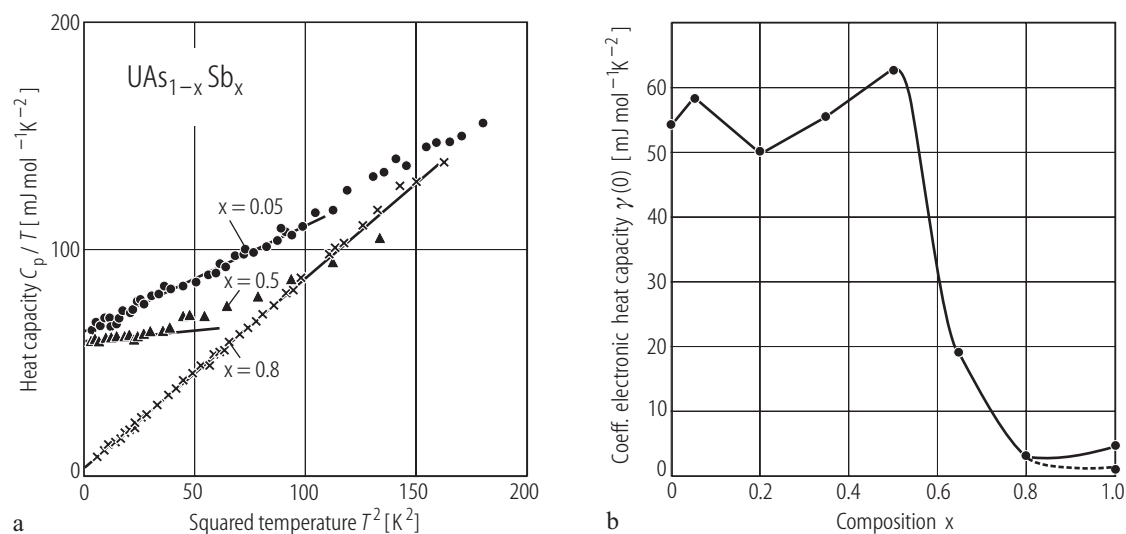


Fig. V.81. U(As,Sb) s.c. (a) The plot C_p/T vs. T^2 in the temperature range 1.5...11 K for three solid solutions $\text{UAs}_{1-x}\text{Sb}_x$ with $x = 0.05, 0.5$ and 0.8 [87ROFV]. The solid lines represent the equation $C_p/T = \gamma(0) + \beta T^2$. For $x = 0.8$ the nuclear Schottky anomaly (C_N) was subtracted.

$C_N(\text{USb}) = 144 \cdot 10^{-3} T^{-2} \text{ J/K mol}$ [85ROV2]. For the remaining compositions no correction of $C_N(T)$ has been used. (b) $\gamma(0)$ vs. x . For $\gamma(0)$ and Θ_D -values see the Table (from [87ROFV]):

x	γ [mJ/molK^2]	Θ_D [K]	Temp. range [K]
0	53.2	221	
0.05	57.9(2.5)	289(10)	1.5...6.3
0.20	49.2(3.5)	192.5(5)	2.5...10
0.35	55.3(3.0)	192(3)	2...9
0.50	62.2(2.0)	203(3)	1.5...8.9
0.65	18.4(5)	161(2)	1.5...11
0.80	3.0(0.5)	169(2)	1.5...10
1.0	4.45*)	168	
	0.20**)	170	1.5...12

Ref.: *) [85ROV2], **) [83RFOV].

For Fig. V.82 see next page

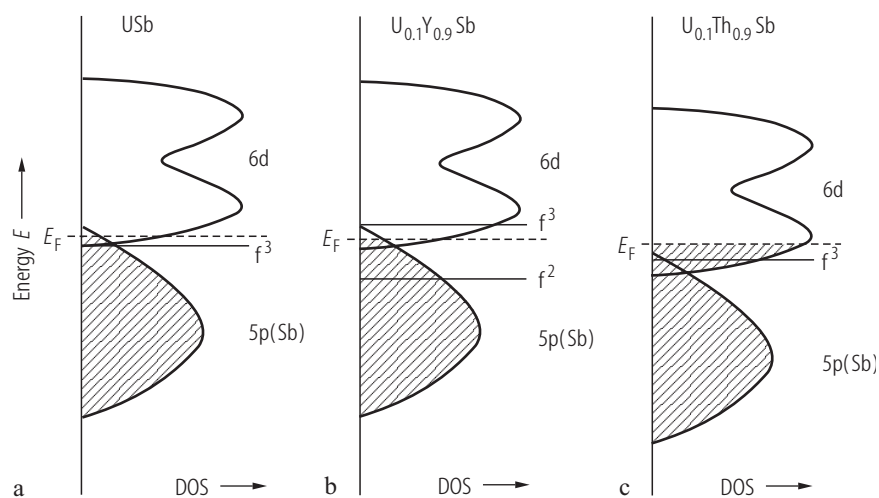


Fig. V.83. $(\text{U,T})\text{Sb}$ ($T = \text{Y, Th}$). Energy level schemes for (a) USb and for dilute solid solutions, (b) $\text{U}_{0.1}\text{Y}_{0.9}\text{Sb}$ and (c) $\text{U}_{0.1}\text{Th}_{0.9}\text{Sb}$ [85SFV]. Shown are only the approximate position of the f states and their width and hybridization effects are omitted. Note that the dilution with either trivalent Y or tetravalent Th affects in different ways the band ground energy E_F .

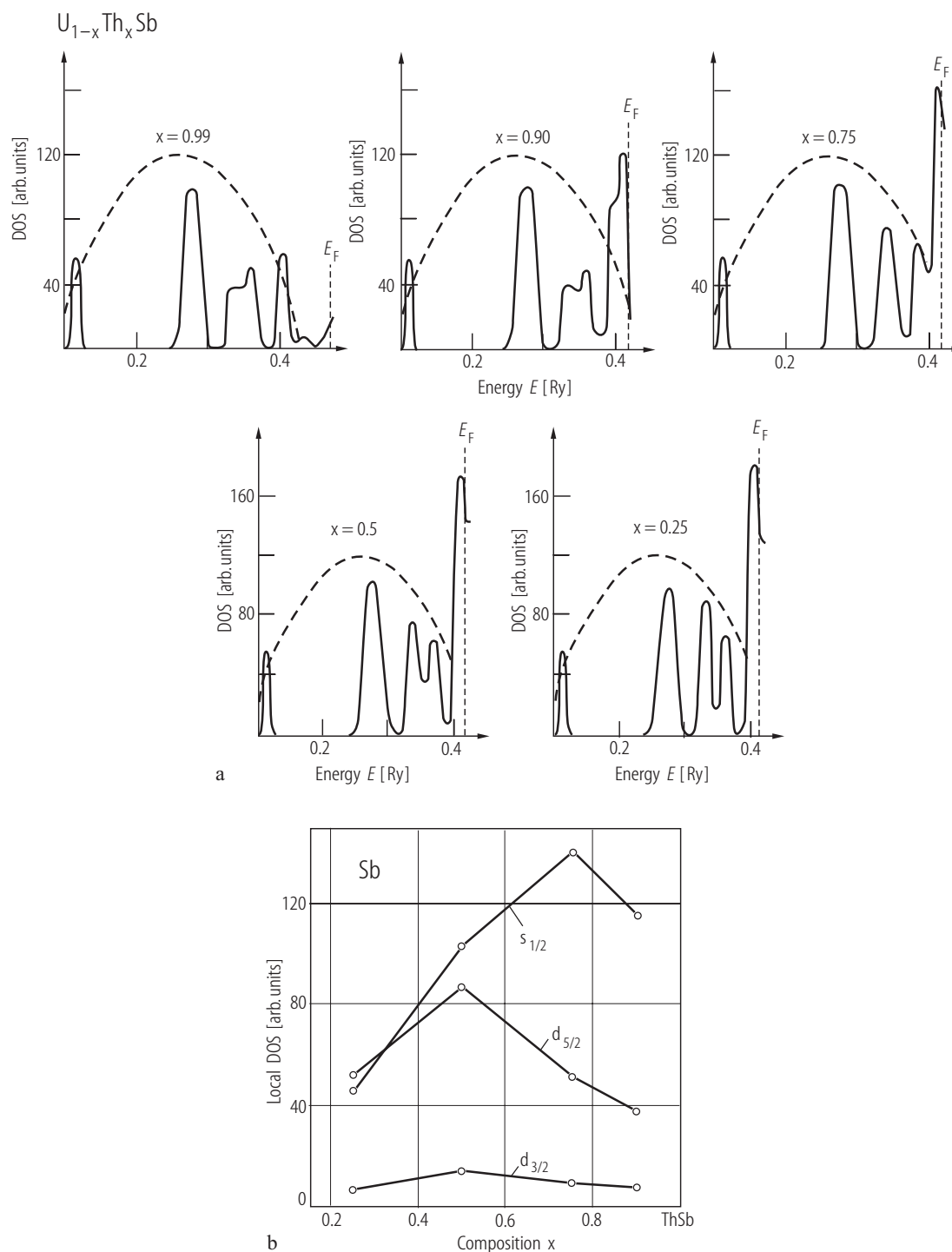


Fig. V.82. (U,Th)Sb. **(a)** The occupied part of the DOS calculated by the fully relativistic KKR-ATA method for the solid solutions $U_{1-x}Th_xSb$ with $x = 0.25, 0.5, 0.75, 0.90$, and 0.99 [80WP]. The dashed line indicates a broad peak of the "Sb-p" band expected in this energy region. One sees that the peak at E_F is substantially increased with decreasing molar fraction x (E_F is almost constant). Note a

rearrangement of the electronic structure from a predominantly "f-band" to a "d-band" compound which is seen by the peak located before E_F . The data can be related to XPS experiment. **(b)** Local DOS of the $s_{1/2}$, $d_{3/2}$ and $d_{5/2}$ states for non-metal (Sb) in the vicinity of E_F as a function of the concentration x [80WP].

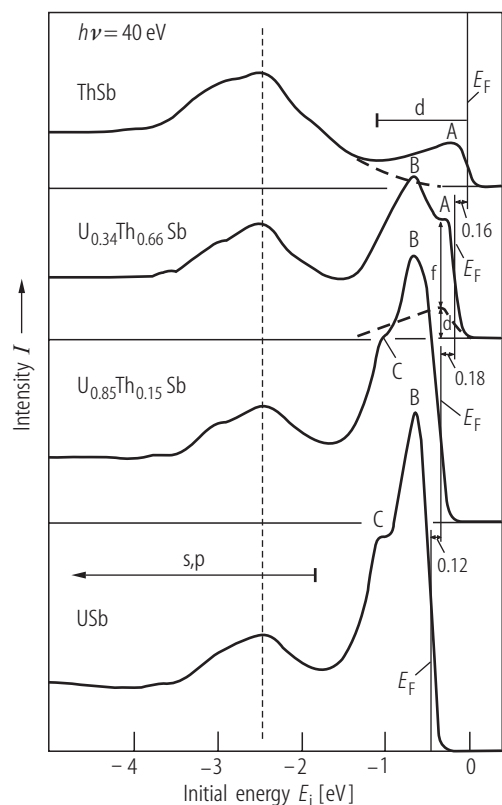


Fig. V.84. (U,Th)Sb s.c. Normalized angle-integrated EDC spectra of the solid solutions $U_{1-x}Th_xSb$ for $x = 0, 0.15, 0.66$ and 1.0 measured at $h\nu = 40$ eV at RT [81RMEV], [82RMV] and [82RMEA]. The spectra are aligned to have the 5p-peak heights coincide. As one sees, the 5f-like spectral peaks coincide as well. In the figure the resulting shifts of E_F are given in eV. In contrast to EBS calculations [80WP], a monotonic increase of E_F with increasing Th concentration x is observed. It shifts upwards by $0.46(2)$ eV on going from USb to ThSb. Peaks A are from the 6d electrons, and the A peak for $x = 0.66$ is equal to that in pure ThSb.

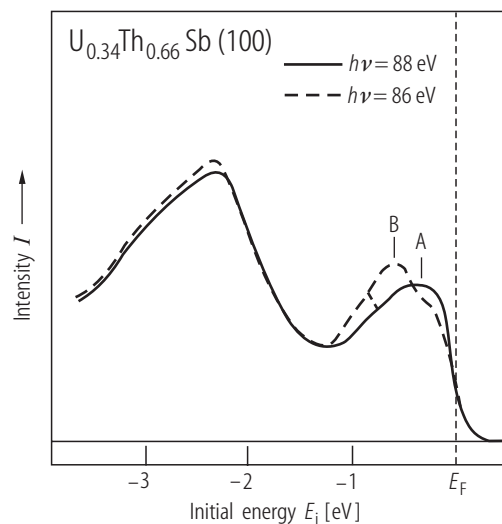


Fig. V.85. (U,Th)Sb s.c. Normalized EDC's for the solid solution $U_{0.34}Th_{0.66}Sb$ taken at $h\nu = 88$ and 86 eV [82RMEA]. Note that the 88 eV spectrum reveals stronger 6d emission (feature A) while that of 86 eV shows a more 5f character (feature B).

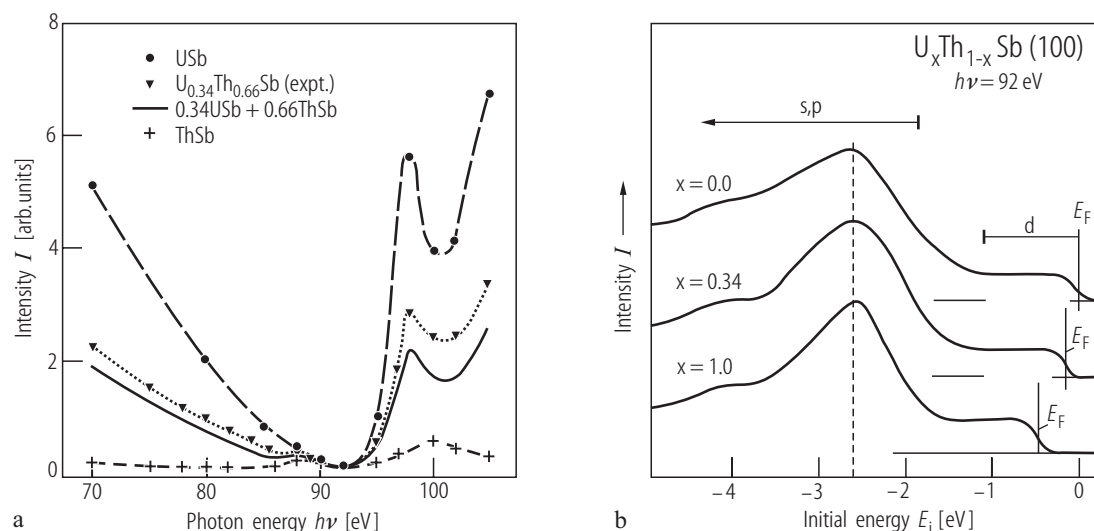


Fig. V.86. (U,Th)Sb s.c. (a) CIS spectra for the solid solution $U_{0.34}Th_{0.66}Sb$ compared to those of USb and ThSb as well as to their superposition [82RMEA]. As seen, the solid solution produces a curve, which shows both the typical USb and ThSb resonance features. (b) The EDC's for the solid solution $U_{0.34}Th_{0.66}Sb$ compared to those of the end compounds USb and ThSb taken at $h\nu=92$ eV

[80BBBP]. This photon energy corresponds to a minimum of the 5f emission due to the 5d \rightarrow 5f resonant excitation. This gives an additional evidence for the presence of 6d band like states. All shown spectra prove a metallic edge at E_F being attributed to occupied 6d electrons (see [81RMEV]).

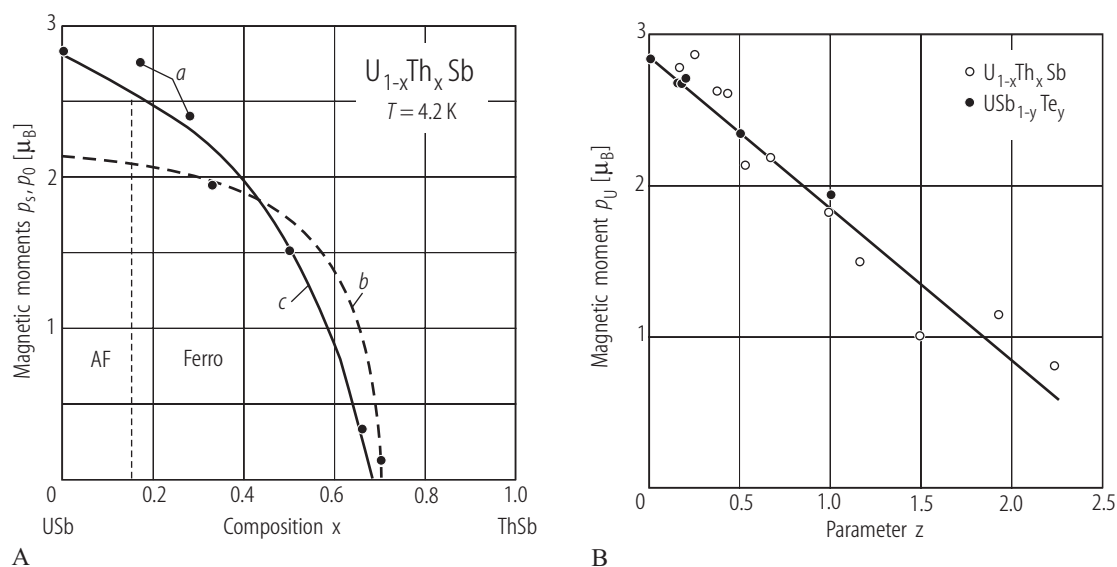


Fig. V.87. (U,Th)Sb. U(Sb,Te). (A) a) Ordered magnetic moment p_O (AF) and p_S (F) (closed circles) of the solid solutions $U_{1-x}Th_xSb$ as a function of Th composition x and b) theoretical description [80CVS2]. For this simple theoretical model in the case of a singlet ferromagnetic state see also [80CVS1]. A gradual (or rapid) valence change from U^{3+} to U^{4+} in the solid solutions is postulated at about $x \geq 0.3$ (dashed line). c) Another simple model based on photoemission findings (solid curve) indicates that uranium retains a constant valence state [81RMEV]. (B) Ordered magnetic moments, p_U , in two solid solutions $U_{1-x}Th_xSb$

(open circles) and $USb_{1-y}Te_y$ (closed circles) obtained from magnetization measurements at $T=4.2$ K and $B=10$ T as a function of parameter z : $z=x/(x-1)$ and $z=y$, respectively [82FSVA]. p_U in USb is taken as $p_0=2.82 \mu_B/U$ at. from neutron diffraction data [76LMSV]. The solid line is a summary variation of calculated moment based on the two equations: 1. $p_U [\mu_B] = [p_0(1-x)-x]/(1-x) = p_0-x/(1-x)$ and 2. $p_U [\mu_B] = p_0-y$, giving the same results (the straight line) under assumptions of a constant uranium valence with $p_0=2.82 \mu_B$ and that each added d-electron by the Th or Te substituted atoms contributes a magnetic moment $p_d=1 \mu_B$.

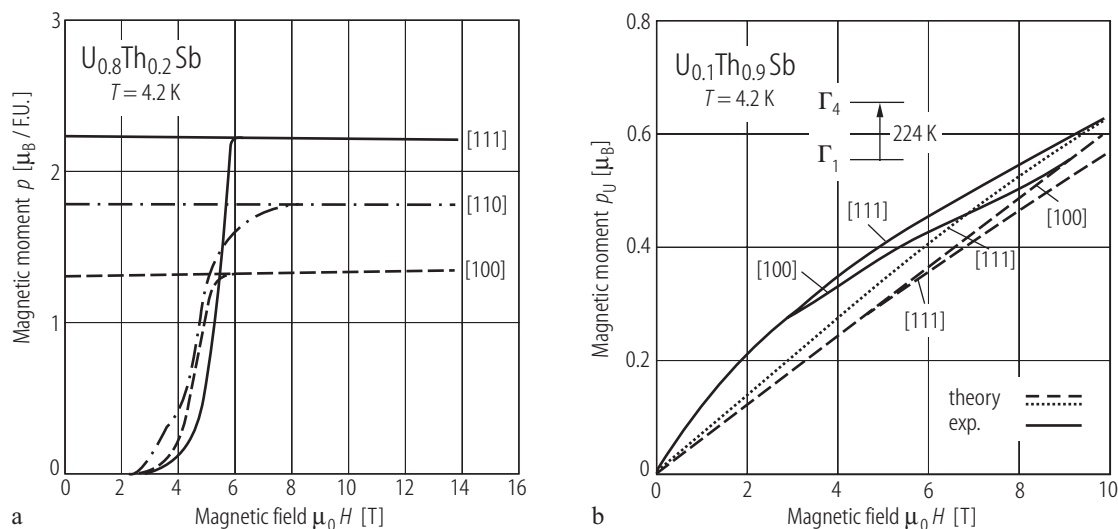


Fig. V.88. (U,Th)Sb s.c. **(a)** Magnetic moment p (in $\mu_B/\text{F.U.}$) vs. applied magnetic field, H , measured at 4.2 K along three main crystallographic directions for the solid solution $\text{U}_{0.8}\text{Th}_{0.2}\text{Sb}$ [79CV]. Note that the primary effect of U/Th substitution is to add one d-conduction electron, thereby changing an antiferromagnet (USb) toward ferromagnetic nature of the magnetic interactions. $p_s = 2.86\ \mu_B/\text{U at}$. The $\cos\theta$ law is followed indicating that a strong anisotropy exists in this solid solution, which holds the easy

magnetization axis along the [111] direction. **(b)** The p_U vs. H curves for $\text{U}_{0.1}\text{Th}_{0.9}\text{Sb}$, which shows the paramagnetic properties at 4.2 K [79CV]. They can be explained only in the frame of the crystal field splitting scheme (shown in the figure) in the case of $5f^2$ configuration (i.e. U^{4+} ion). LLW parameters $x = -1$, $W = 16.0\text{ K}$; $\lambda_{\text{ex}} = 22.7\text{ T}/\mu_B$ (long dashed line), $\lambda = 24.9\text{ T}/\mu_B$ (dotted line) for [111] (see also Fig. III.64b).

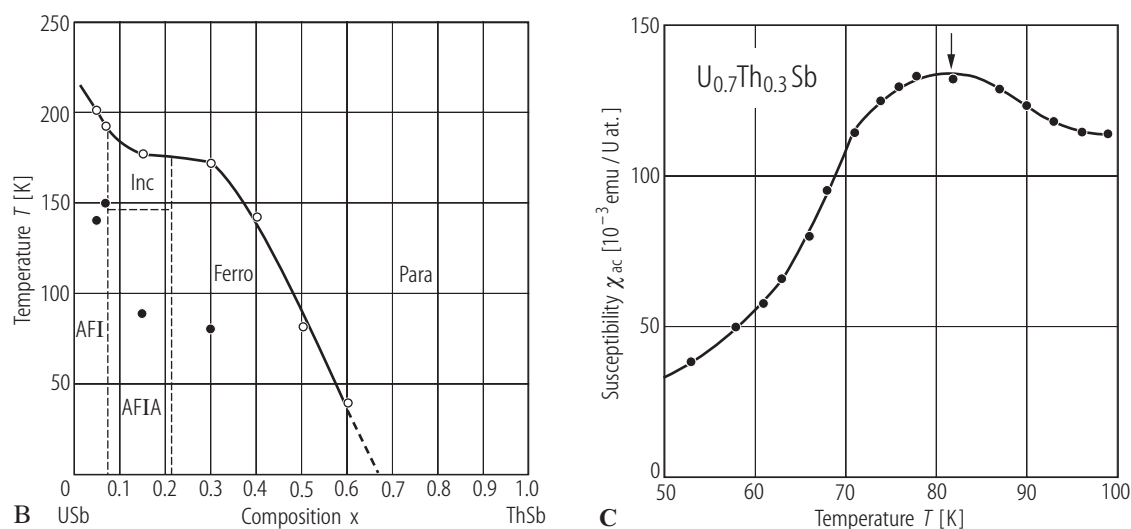


Fig. V.89B, C. For caption see next page

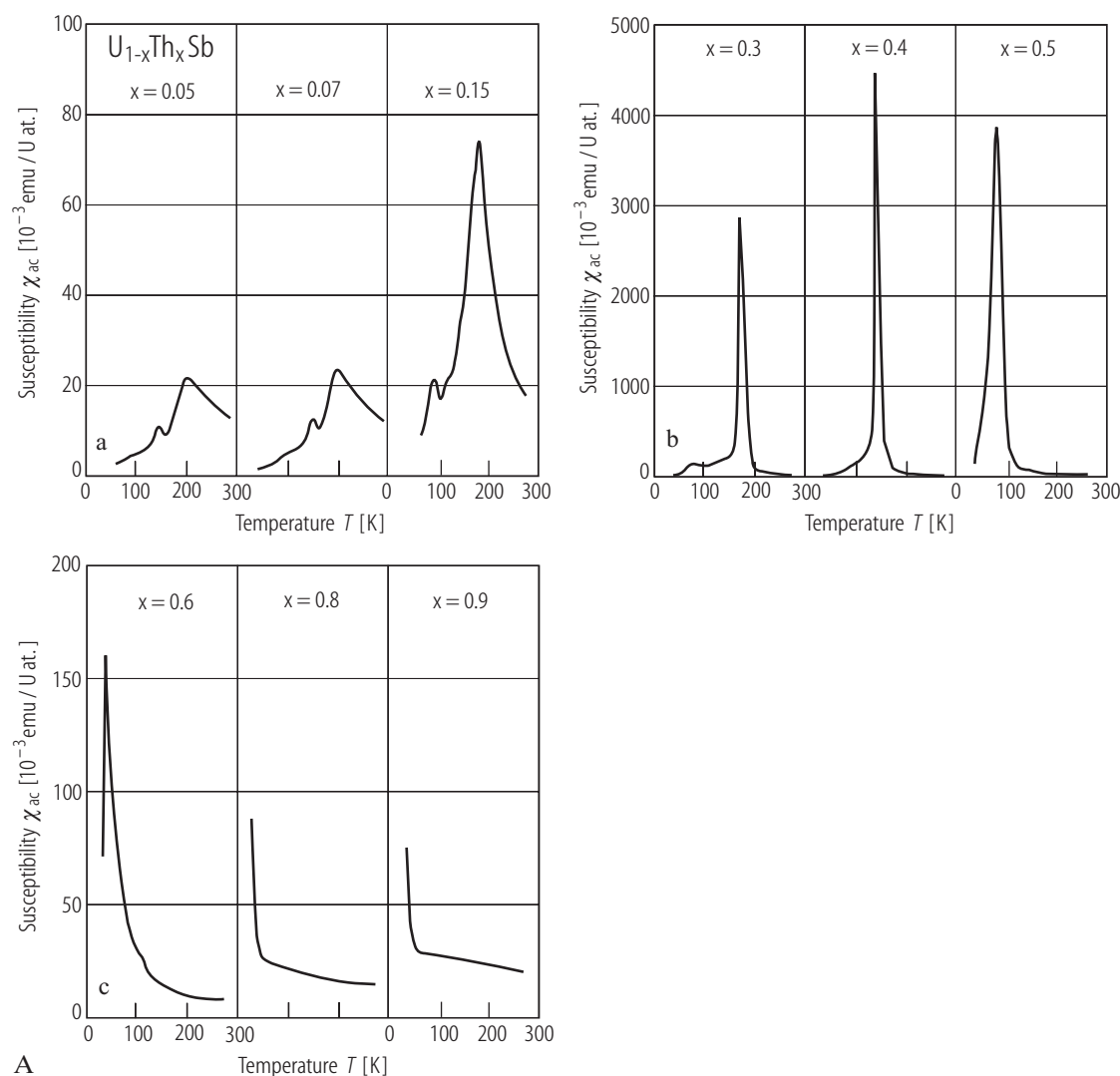


Fig. V.89. (U,Th)Sb. **(A)** ac susceptibility, χ_{ac} , vs. temperature, T , for the solid solutions $U_{1-x}Th_xSb$, where **(a)** $x = 0.05, 0.07, 0.15$ and **(b)** $x = 0.3, 0.4$ and 0.5 and **(c)** $x = 0.6, 0.8$ and 0.9 [86TBBV]. Note that for the compositions with $x \leq 0.15$ two peaks are found. The higher temperature peaks for $x = 0.05$ and 0.07 correspond to the respective T_N 's while the lower temperature peaks located near 150 K are not associated with any phase change described in the MPD (see Fig. V.91). For $x = 0.15$ even two such peaks are observed around $T \sim 100$ K. In turn, the sharp $\chi_{ac}(T)$ peaks for $x \geq 0.3$ correspond to the respective ordering temperatures. **(B)** (T, x) MPD determined on the basis of

ac susceptibility measurements [86TBBV]. The closed circles mark the temperatures of observed additional maxima in the $\chi_{ac}(T)$ curves. The dashed lines delimit the presence of the antiferromagnetic phases AF I, AF IA and incommensurate (Inc) phase, found in neutron diffraction experiments by [80BQRV], on which the MPD has been constructed and is presented in Fig. V.91. It is interesting to note that no characteristic peak in $\chi_{ac}(T)$ is found at the commensurate-incommensurate transition temperature, T_{IC} , of 150 K. **(C)** An additional peak for $x = 0.3$ at 82 K being detected without ambiguity on the $\chi_{ac}(T)$ curve is of unknown origin [86TBBV].

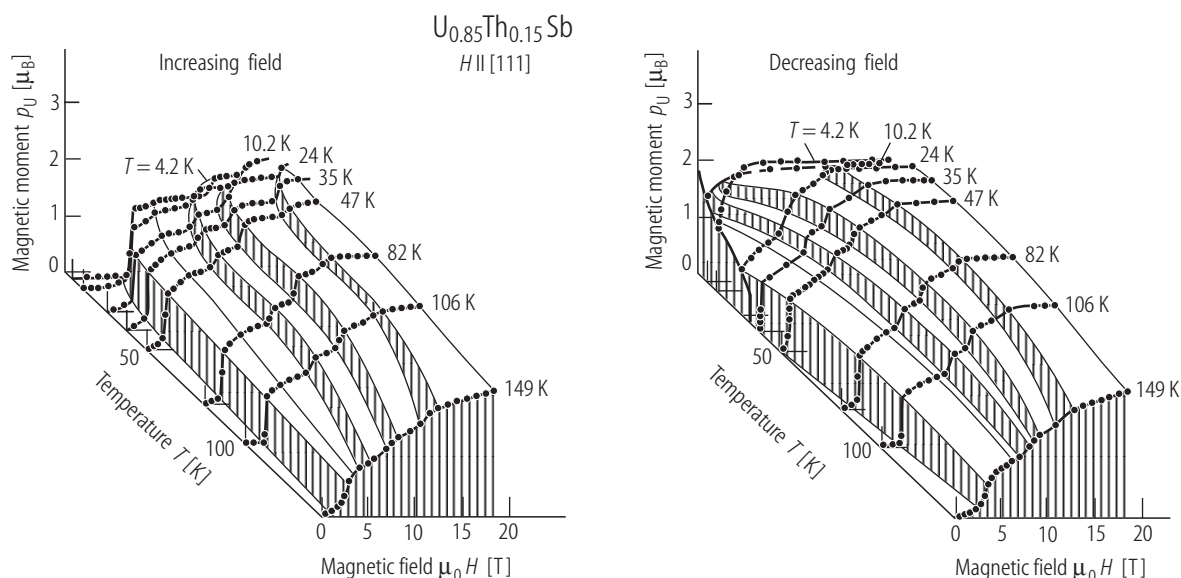


Fig. V.90. (U,Th)Sb s.c. Magnetic moment per U atom, p_U , vs. applied magnetic field, H , measured at various temperatures T (indicated) for the solid solution $U_{0.85}Th_{0.15}Sb$. $H \parallel [111]$. The increasing (lhs) and decreasing (rhs) runs of magnetic field were used [82RBQV]. Note a large number

of magnetization steps, which gradually are revealed by magnetization before its saturation. They correspond to the following net values: $1/3$, $1/2$, $2/3$ and $5/6$ with respect to a saturation value p_s .

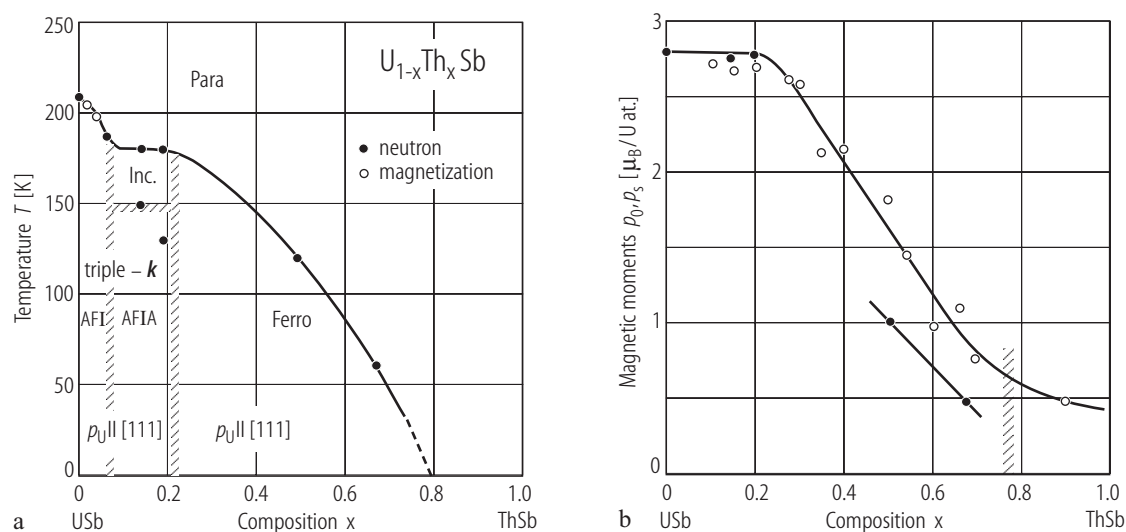


Fig. V.91. (U,Th)Sb. s.c. **(a)** (T, x) MPD of $U_{1-x}Th_xSb$ solid solutions determined by neutron and magnetization measurements [82RBQV]. The phase type I disappears for $x > 0.07$ and the ferromagnetic state for $x > 0.25$ occurs. For compositions between, an incommensurate order develops at T_N , which locks into a triple- k type IA phase at temperatures below about 150 K. However, a different ground state is proposed in studies [93PLTS] for $x = 0.15$, see Fig. V.94.

(b) Magnetic moments p_0 (AF region) and p_s (F region) vs. composition [82RBQV]. It remains in AF structures nearly constant (e.g. $p_0 = 2.75(1) \mu_B$ for $x = 0.15$), while in the ferromagnetic state it decreases almost linearly with increasing x . Doping tetravalent Th^{4+} into trivalent USb adds one electron per Th atom to the conduction band which drives the system to ferromagnetism (see e.g. [91SC1,2]).

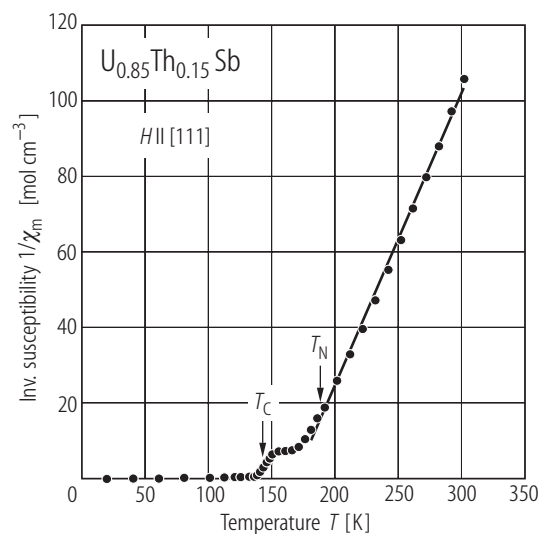


Fig. V.92. (U,Th)Sb s.c. Inverse molar magnetic susceptibility, χ_m^{-1} , of the solid solution $\text{U}_{0.85}\text{Th}_{0.15}\text{Sb}$ vs. temperature, T , measured for $H \parallel [111]$ at 0.3 T [93PLTS]. At temperatures $T > 190$ K $p_{\text{eff}} = 3.50(5) \mu_B/\text{U at.}$, $T_C = 145$ K and $T_N = 190$ K.

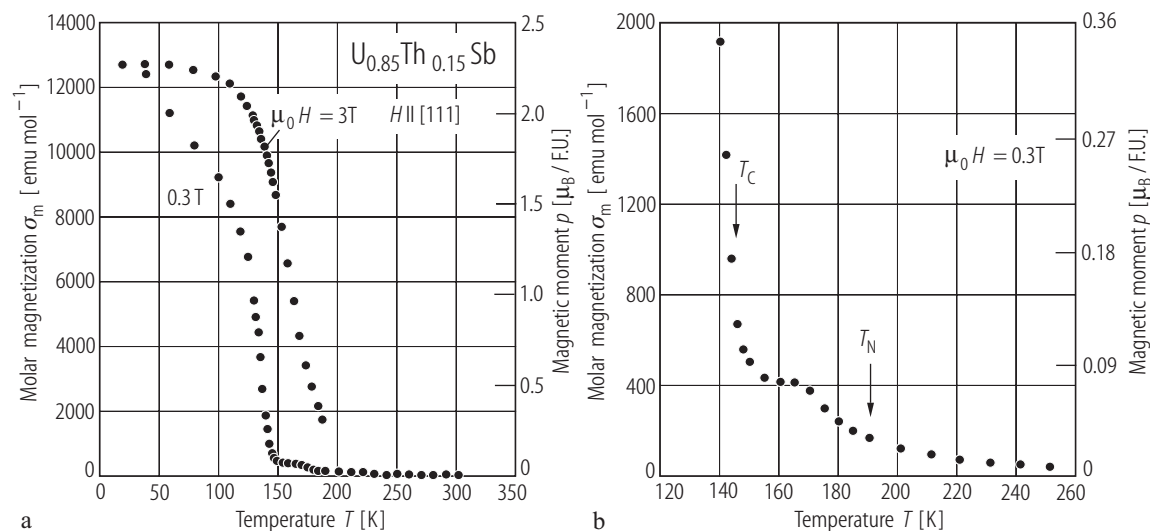


Fig. V.93. (U,Th)Sb s.c. Molar magnetization, σ_m , (magnetic moment in μ_B per formula unit) for the solid solution $\text{U}_{0.85}\text{Th}_{0.15}\text{Sb}$ measured along the $[111]$ direction at temperatures around T_C ($= 145$ K) and T_N ($= 190$ K) and in applied magnetic fields of (a) 0.3 and 3 T and (b) enlarged

at 0.3 T [93PLTS]. $p_S = 2.3 \mu_B/\text{F.U.}$ which corresponds to $2.7 \mu_B/\text{U at.}$ Compare these values with those given by [82RBQV]. Note that the antiferromagnetic state is quenched by fields as high as 3 T.

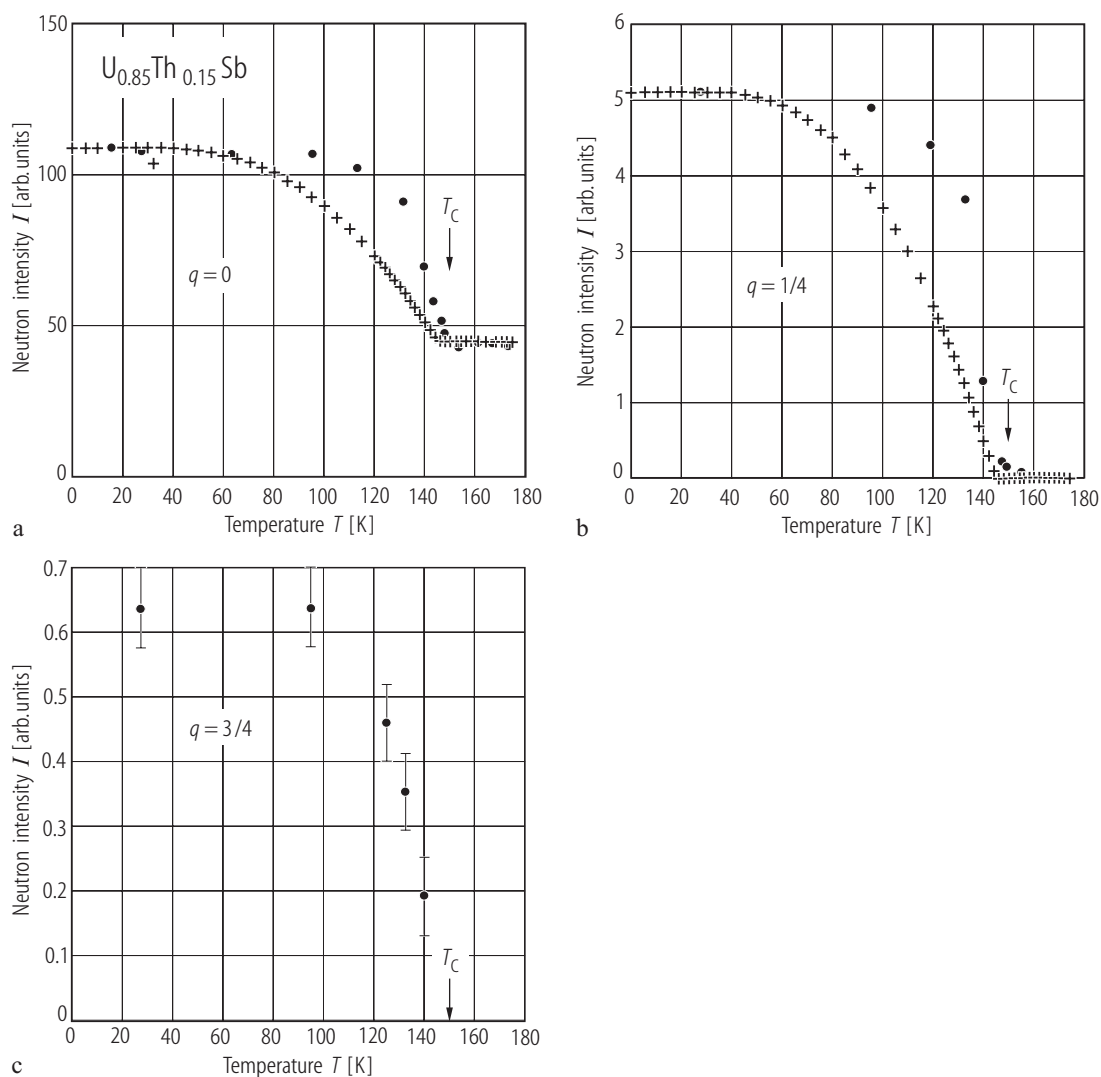


Fig. V.94. (U,Th)Sb s.c. Neutron intensity, I , (in arbitrary scale) vs. temperature, T , for the solid solution $\text{U}_{0.85}\text{Th}_{0.15}\text{Sb}$ measured for the three major components: **(a)** (111) nuclear reflection which has ferromagnetic contribution ($q = 0$), and modulation components: **(b)** $q = 1/4$ and **(c)** $q = 3/4$ observed at temperatures $T \leq T_c$ ($= 145$ K) [93PLTS]. The

crosses give the square of the Brillouin function ($S = 1/2$), which show an abruptness of the measured T dependences, being essentially the same for each component. This magnetic structure is inconsistent with that in the MPD (Fig. V.91) for $x \approx 0.15$.

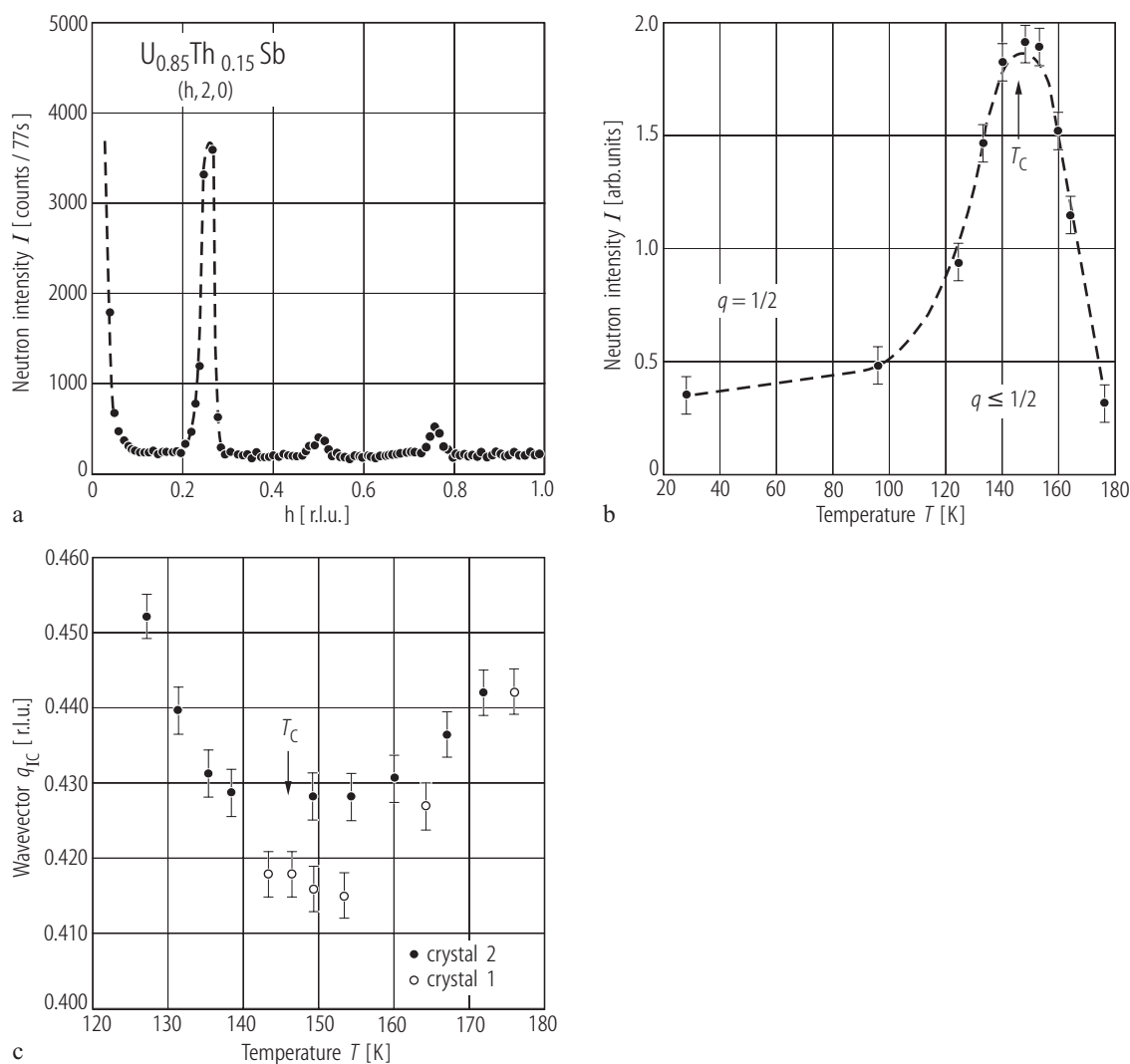


Fig. V.95. (U,Th)Sb. s.c. (a) Neutron diffraction scans of $\text{U}_{0.85}\text{Th}_{0.15}\text{Sb}$ measured at $T = 89$ K (ferromagnetic order) along the reciprocal lattice line $(h, 2, 0)$, the three components at $q = 1/4, 1/2$ and $3/4$ are present (see also Fig. V.94) [93PLTS]. (b) Total neutron intensity, I , vs. temperature, T , measured in the range $0.45 < h < 0.55$ (see

figure (a)) [93PLTS]. This shows developing of $q_{IC} < 1/2$ intensity with increasing temperature. (c) The incommensurate wave vector q_{IC} as a function of temperature, T , around $T_C (= 145$ K) for the two single crystals examined [93PLTS].

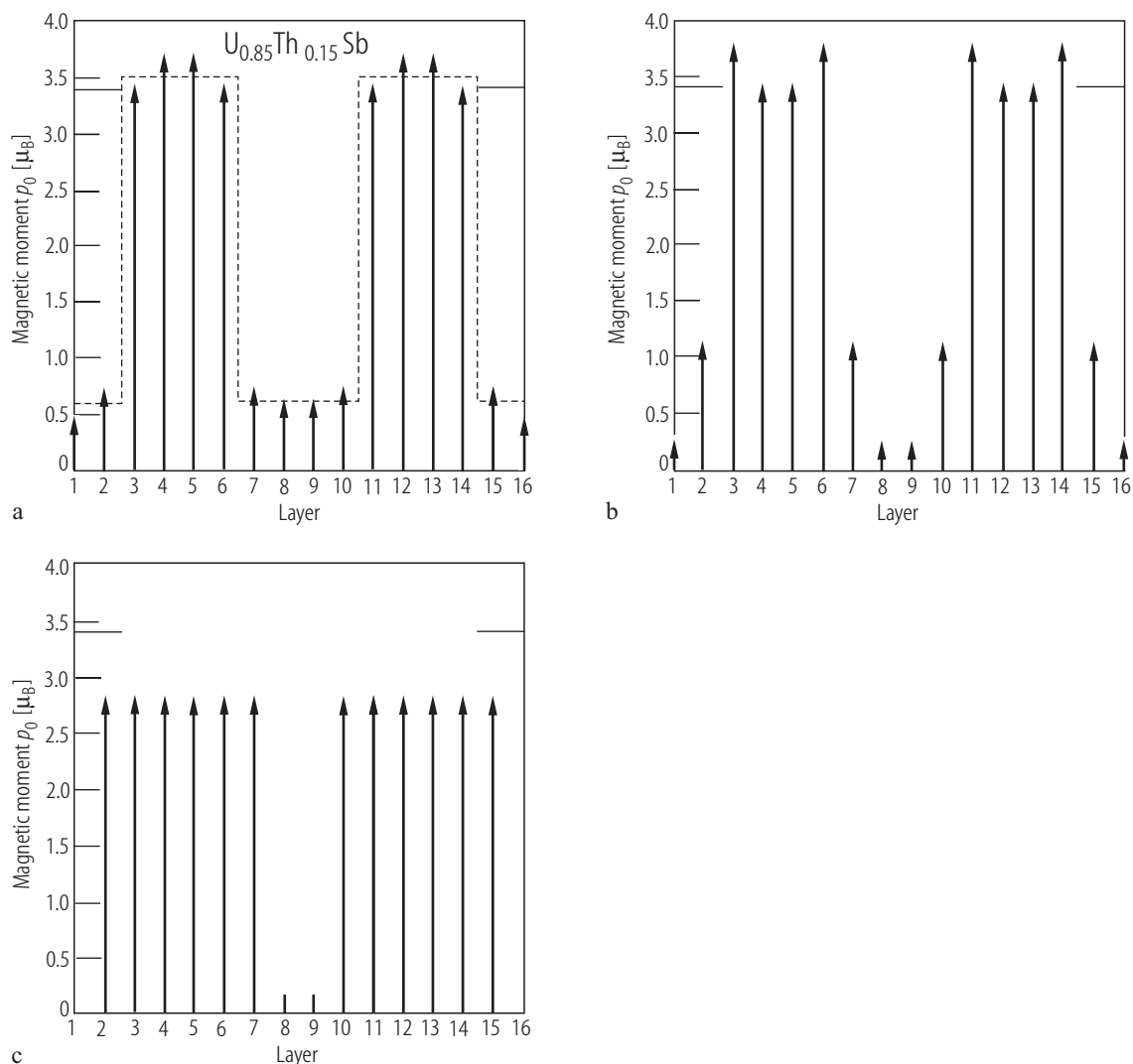


Fig. V.96. (U,Th)Sb s.c. The most probable longitudinal magnetic structure models in the transverse presentation for the solid solution $U_{0.85}Th_{0.15}Sb$ [93PLTS]. **(a)** The "almost" square wave (dashed line) where the component $q = 1/2$ is

omitted, **(b)** the component $q = 1/2$ is added-the square wave is distorted, **(c)** a possible configuration 6+, 0, 0 derived from the X-ray amplitudes (see Fig. V.97). The maximum possible moment of uranium $p_0 \approx 3.4 \mu_B$.

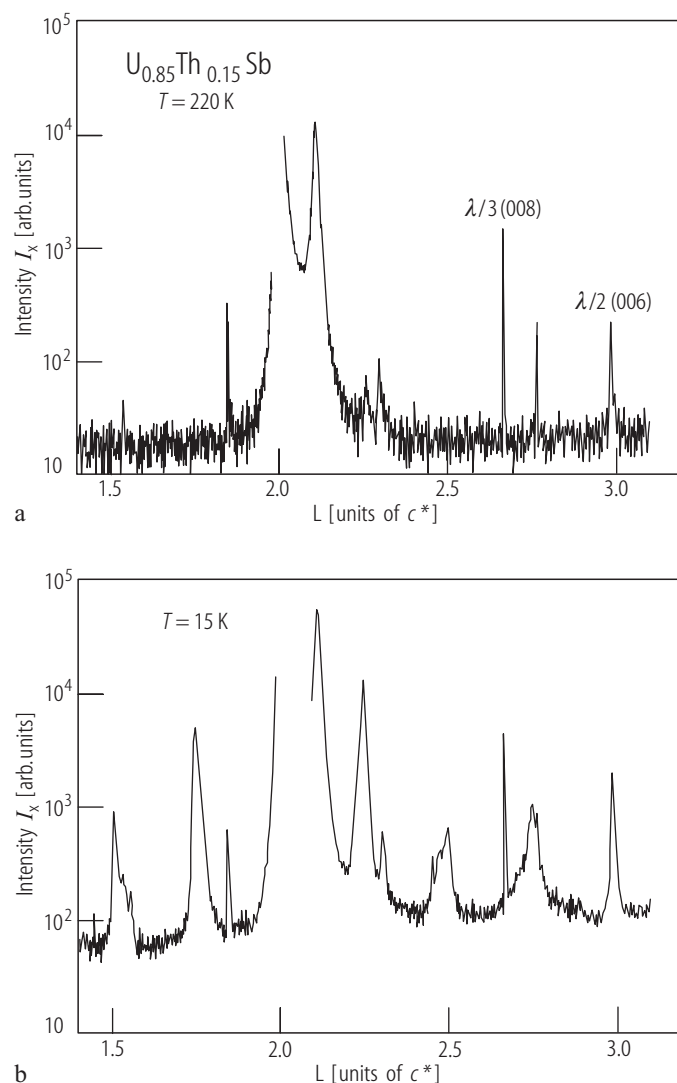


Fig. V.97. (U,Th)Sb s.c. RXMS: Magnetic X-ray scans. Intensity (as $\log I_x$) measured along the [001] direction at (a) 220 K (above T_N) and (b) 15 K (below T_N) for the solid solution $U_{0.85}Th_{0.15}Sb$. The narrow peaks in the 220 K-pattern, apart from the very strong ($L = 2$) charge peak, are due to nonmagnetic effects. Note a number of new peaks of magnetic origin in the 15 K-pattern, but out of ferromagnetic components (usually not seen). Comparing to neutron scattering results, the q -space resolution with X-rays is about four times better and the X-ray magnetic satellite intensities are much stronger [93PLTS].

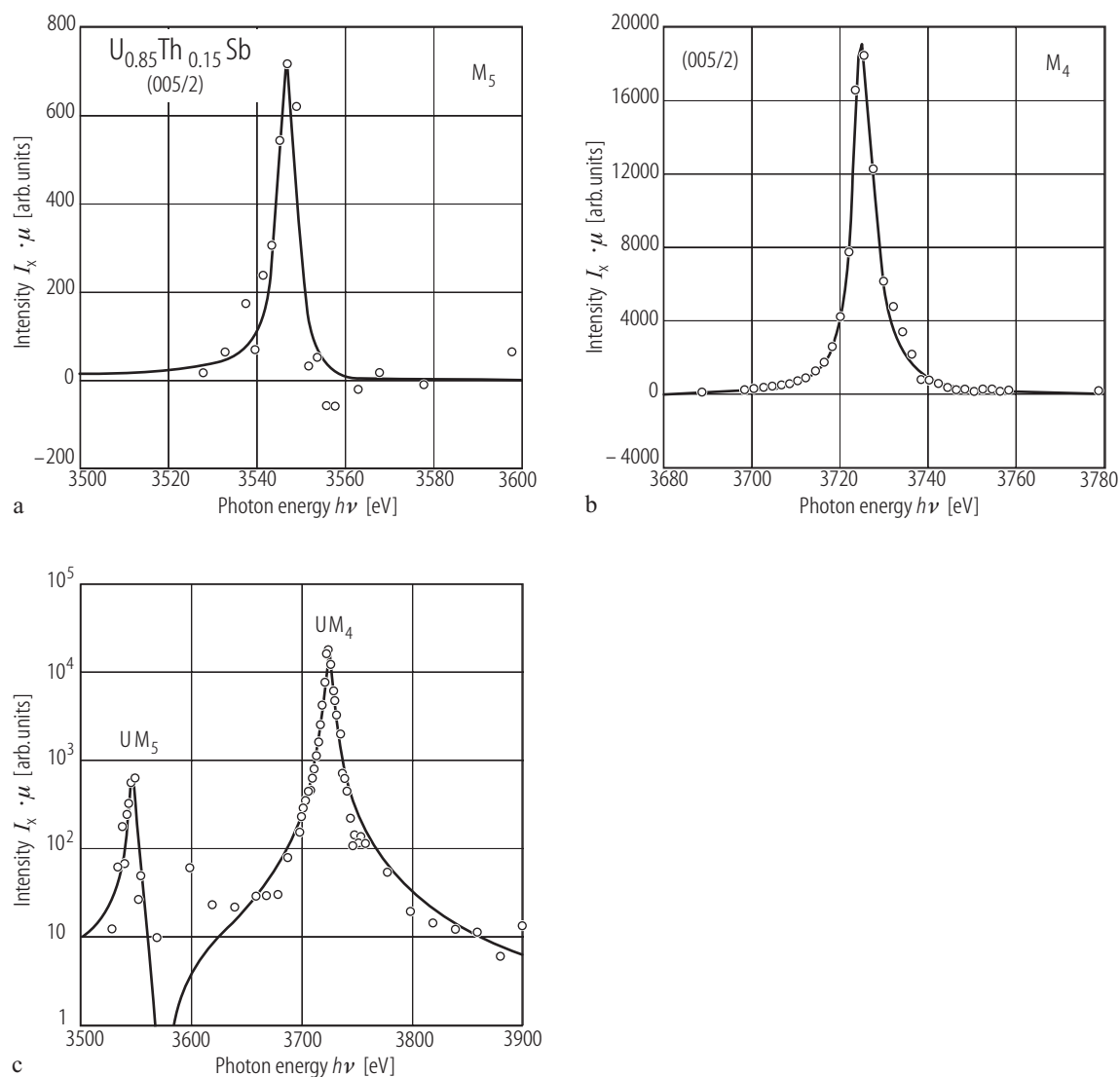


Fig. V.98. (U,Th)Sb s.c. RXMS: Energy dependence of the integrated X-ray intensity of the (0 0 5/2) magnetic reflection at 12 K of the solid solution $U_{0.85}Th_{0.15}Sb$ for the two resonance edges: **(a)** M_5 and **(b)** M_4 [92TSLG]. **(c)** The X-ray intensity (log scale) of M_4 and M_5 data corrected for

absorption vs. photon energy, $h\nu$, [92TSLG]. The solid lines are fits of the M_5 and M_4 data to standard formulas for atomic resonances, where these are considered as two resonances, each with amplitudes A_4 and A_5 , widths Γ_4 and Γ_5 and energies E_4 and E_5 , respectively.

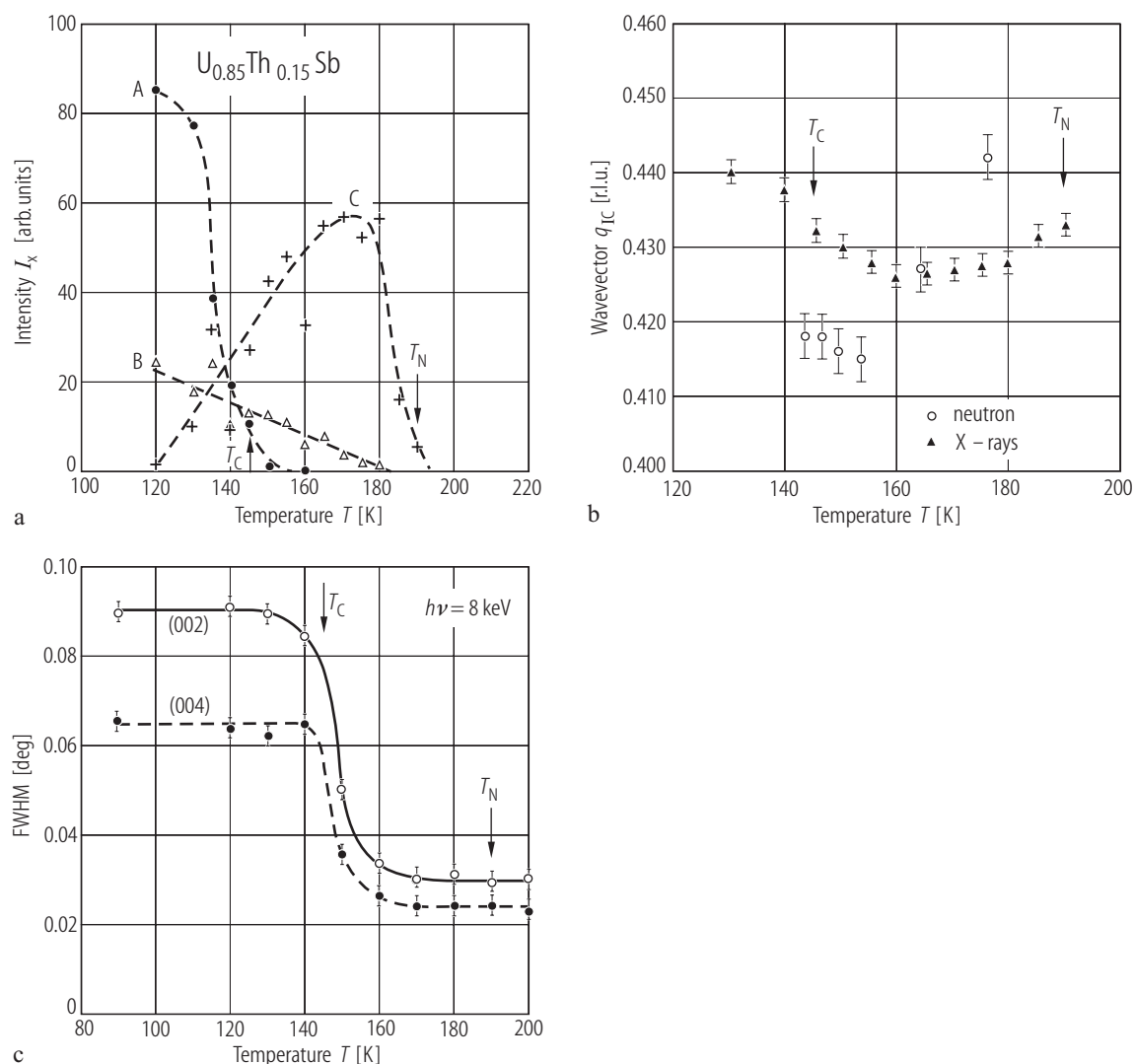


Fig. V.99. $(\text{U,Th})\text{Sb}$ s.c. RXMS: **(a)** Integrated X-ray intensity, I_x , of the three major components of the magnetic structure of $\text{U}_{0.85}\text{Th}_{0.15}\text{Sb}$ as a function of temperature T [93PLTS]. Component A (magnetic structure $(4+, 4-)$ with $q = 1/4$ and $3/4$), component B (magnetic structure $(2+, 2-)$ with $q = 1/2$), component C (incommensurate q_{1C}). In comparison to neutron experiment the difference occurs for the $q = 1/2$ component only, which is considerably stronger in the X-ray case. The difference originates from the fact, that X-rays are probing the “near surface” behaviour only

(about 400 nm), which may influence the “body” structure. **(b)** The incommensurate wave vector q_{1C} vs. temperature, T , measured on the same $\text{U}_{0.85}\text{Th}_{0.15}\text{Sb}$ crystal (crystal 1) by both neutrons (open circles) and X-ray resonance (closed triangles) [93PLTS]. **(c)** Transverse FWHM of the (002) and (004) reflections as a function of temperature, T , around T_C ($= 145$ K) studied by X-ray scattering [93PLTS]. The broadening of transverse, but not longitudinal widths is ascribed as a finite-size effect of the magnetic domains (see the original paper).

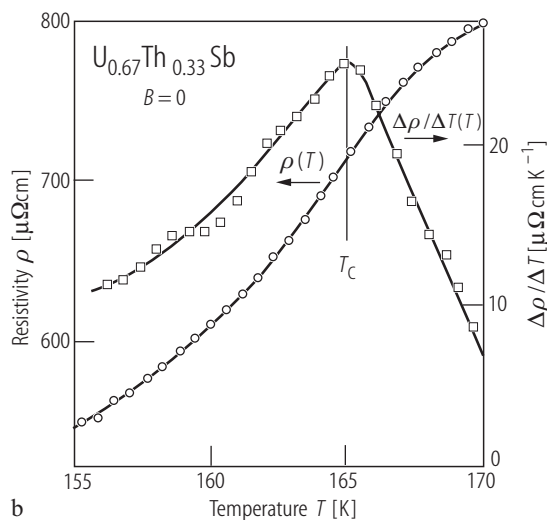
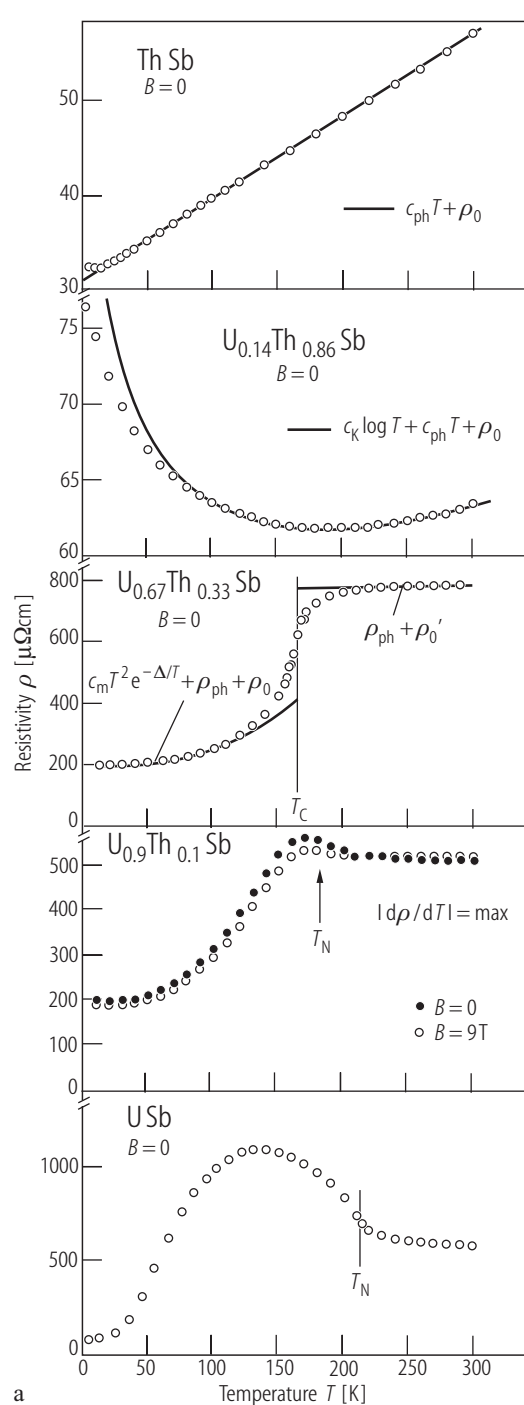


Fig. V.100. $U_{1-x}Th_xSb$. s.c. **(a)** Electrical resistivity, ρ , vs. temperature, T , of the solid solutions $U_{1-x}Th_xSb$ for $x = 0, 0.1, 0.33, 0.86$ and 1.0 [82FSVA]. The solid lines are described by corresponding equations as displayed. For $x = 0.33$, T_C is determined as the maximum in the temperature derivative of the resistivity (see Fig. **(b)**). For characteristic data see the Table below. **(b)** Electrical resistivity, ρ , (lhs) and its temperature derivative $\Delta\rho(T)/\Delta T$ (rhs) for the ferromagnet $U_{0.67}Th_{0.33}Sb$ around the Curie temperature T_C [82FSVA]. $T_C \approx 165(1)$ K. Note that the temperature derivative of the resistivity indicates an inflection point in the $\rho(T)$ curve at T_C .

Footnotes of Table: *)The conduction electron concentration for a single-band model. **) $\Delta = 12$ meV.

x	Magnetic order	T_C, T_N [K]	ρ (4.2 K) [$\mu\Omega\text{cm}$]	ρ (300 K) [$\mu\Omega\text{cm}$]	$N^*)$ [$e^-/\text{f.u.}$]
0	AF	215 ± 2	80-120	600...650	—
0.1	AF	183 ± 5	197	510	0.1
0.33**)	F	165 ± 1	196	790	~ 0.5
0.86	para	—	77	64	—
1.0	para	—	32	56	1.48